

Resolving the dusty star-forming galaxy GN20 at $z = 4.055$ with NOEMA and JWST: A similar distribution of stars, gas and dust despite distinct apparent profiles

LEINDERT A. BOOGAARD ,¹ FABIAN WALTER ,^{2,3} AXEL WEIS ,⁴ LUIS COLINA ,⁵ JACQUELINE HODGE ,¹ ARJAN BIK ,⁶
 ALEJANDRO CRESPO GÓMEZ ,⁷ EMANUELE DADDI ,⁸ GEORGIOS E. MAGDIS ,^{9,10,11} ROMAIN A. MEYER ,¹² AND GÖRAN ÖSTLIN ¹⁰

¹Leiden Observatory, Leiden University, PO Box 9513, NL-2300 RA Leiden, The Netherlands

²Max Planck Institute for Astronomy, Königstuhl 17, 69117 Heidelberg, Germany

³National Radio Astronomy Observatory, Pete V. Domenici Array Science Center, P.O. Box O, Socorro, NM 87801, USA

⁴Max Planck Institute for Radiosastronomie, Auf dem Hügel 69, 53121 Bonn, Germany

⁵Centro de Astrobiología (CAB), CSIC-INTA, Ctra. de Ajalvir km 4, Torrejón de Ardoz, E-28850, Madrid, Spain

⁶Department of Astronomy, Stockholm University, Oscar Klein Centre, AlbaNova University Centre, 106 91 Stockholm, Sweden

⁷Space Telescope Science Institute (STScI), 3700 San Martin Drive, Baltimore, MD 21218, USA

⁸CEA, IRFU, DAp, AIM, Université Paris-Saclay, Université Paris Cité, Sorbonne Paris Cité, CNRS, 91191 Gif-sur-Yvette, France

⁹Cosmic Dawn Center (DAWN), Denmark

¹⁰DTU Space, Technical University of Denmark, Elektrovej, Building 328, 2800, Kgs. Lyngby, Denmark

¹¹Niels Bohr Institute, University of Copenhagen, Jagtvej 128, 2200 Copenhagen, Denmark

¹²Departement d'Astronomie, University of Geneva, Chemin Pegasi 51, 1290 Versoix, Switzerland

(Received August 5, 2025; Revised October 7, 2025; Accepted October 17, 2025)

ABSTRACT

We present high-resolution ($0''.13$ – $0''.23$) NOEMA observations of the dust continuum emission at 1.1 mm (rest-frame 220 μ m) and JWST/NIRCam and MIRI imaging of the $z = 4.055$ starburst galaxy GN20. The sensitive NOEMA imaging at 1.6 kpc resolution reveals extended dust emission, ≈ 14 kpc in diameter ($r_e \approx 2.5$ kpc, $b/a = 0.5$), that is centrally asymmetric and clumpy. The dust emission is as extended as the stellar emission and the molecular gas traced by ^{12}CO (2–1), with a common center, and is brightest in the strongly-obscured nuclear part of the galaxy. Approximately one-third of the total dust emission emerges from the nucleus and the most prominent clump to the south, and (only) 60% from the central 3.5×1.5 kpc ($0''.5$ – $0''.2$), implying that the starburst is very extended. The combined JWST and NOEMA morphology suggests GN20 experienced a recent interaction or merger, likely invigorating the starburst. The radial surface brightness profiles of the molecular gas and near-infrared stellar emission are similar, while in contrast, the dust emission appears significantly more concentrated. Through self-consistent radiative transfer modeling of the integrated and resolved ^{12}CO and dust emission, we derive an $M_{\text{mol}} = 2.9_{-0.3}^{+0.4} \times 10^{11} \text{ M}_\odot$ with $\alpha_{\text{CO}} = 2.8_{-0.3}^{+0.5}$. We find the extended dust implies a lower global dust optical depth than previously reported, but a high dust mass of $M_{\text{dust}} = 5.7_{-0.6}^{+0.8} \times 10^9 \text{ M}_\odot$ and gas-to-dust ratio of ≈ 50 . Furthermore, we show that the distinct apparent radial profiles of the gas and dust can be explained purely by radiative transfer effects (differences in the radial optical depths and temperatures) and the observations are consistent with the gas and dust mass being similarly distributed throughout the starburst. The latter highlights the importance of accounting for radiative transfer effects when comparing molecular gas and dust distributions from different tracers.

Keywords: Dust continuum emission (412), Galaxy structure (622), High-redshift galaxies (734), Millimeter astronomy (1061), James Webb Space Telescope (2291)

1. INTRODUCTION

Corresponding author: Leindert Boogaard
 boogaard@strw.leidenuniv.nl

Dusty star-forming galaxies represent some of the most intense starbursts in the universe, making them a unique laboratory to study the environment for star formation in the

early universe (Casey et al. 2014; Hodge & da Cunha 2020). The spatial distribution of the dust, gas and stars holds important clues to the triggering mechanism of the starbursts (e.g., mergers, interactions, accretion events) and, more generally, provides key constraints for resolved predictions from theoretical models of galaxy formation (e.g., Cochrane et al. 2019; Popping et al. 2022).

The advent of sensitive, ground-based sub-mm interferometers (ALMA, NOEMA) has enabled resolved studies of the dust continuum and molecular gas emission on (sub)kpc scales in dusty star-forming galaxies (e.g., Simpson et al. 2015; Hodge et al. 2016; Gullberg et al. 2019). However, due to their large volumes of gas and dust, the resolved stellar structure has remained largely obscured. The latter has now changed thanks to JWST, which can peer through the dust and spatially resolve the stellar structure of gas-rich galaxies across the main-sequence on (sub)kiloparsec scales (e.g., Cheng et al. 2022; Álvarez-Márquez et al. 2023; Colina et al. 2023; Huang et al. 2023; Gillman et al. 2023, 2024; Boogaard et al. 2024; Hodge et al. 2025). For dusty star forming galaxies, resolved studies have shown that the low- J ^{12}CO emission tracing the molecular gas is often extended, similar to the starlight, while the dust continuum is observed to be more compact (Hodge et al. 2015; Chen et al. 2017; Calistro Rivera et al. 2018; Tadaki et al. 2020; Ikeda et al. 2022; Tadaki et al. 2023).

GN20 is a prototypical, massive dusty star forming galaxy at a redshift of 4.055, about 1.5 billion years after the big bang. It is a bright submillimeter galaxy ($f_{850\mu\text{m}} = 20\text{ mJy}$) with a total infrared luminosity of about $L_{\text{IR}} = 1.5 \times 10^{13} L_{\odot}$ (Tan et al. 2014; Cortzen et al. 2020), located in an overdensity or protocluster (Pope et al. 2005, 2006; Daddi et al. 2009; Carilli et al. 2011). The bulk of the galaxy is completely obscured at rest-frame UV/optical wavelengths, with only an arc of UV-bright emission showing at a distance of about 4 kpc from the center (Carilli et al. 2010; Hodge et al. 2012, 2015). The molecular gas is distributed in an extended clumpy structure with a diameter of 14 ± 4 kpc, with a total molecular gas mass of $M_{\text{mol}} = (1.3 \pm 0.4) \times 10^{11} (\alpha_{\text{CO}}/0.8) M_{\odot}$ (Hodge et al. 2012, cf. Carilli et al. 2010) and the molecular and ionized gas kinematics are consistent with a rotating disk with $M_{\text{dyn}} \approx 5 \times 10^{11} M_{\odot}$ (Hodge et al. 2012; Bik et al. 2024; Übler et al. 2024). High-resolution PdBI dust-continuum observations at $880\mu\text{m}$ revealed a bright dusty starburst centered on the molecular gas reservoir and elongated in the north-south direction (Hodge et al. 2015), but not as extended as the molecular gas disk, though the extended emission may have been missed due to limited sensitivity in combination with a dust temperature gradient.

Recent rest-frame $1.1\mu\text{m}$ imaging with JWST/MIRI (Colina et al. 2023) spatially resolved the stellar structure for the first time, finding it extends over a similar region as the molec-

ular gas, with an unresolved nucleus offset by about 1 kpc from the center of what appears as a stellar disk with an effective radius of $r_e = 3.6\text{ kpc}$ (axis ratio $b/a = 0.8$). The offset nucleus suggests that GN20 is, or has been, involved in an interaction or merger event, which is not unexpected given it is the brightest galaxy in a protocluster (Colina et al. 2023). The total stellar mass of the system is $M_* = (8.6 \pm 4.3) \times 10^{10} M_{\odot}$ with a star formation rate (SFR) of $2550 \pm 150 M_{\odot} \text{ yr}^{-1}$ (Crespo Gómez et al. 2024, cf. Tan et al. 2014). Pa α observations with the MIRI MRS showed a clumpy structure that extends out to about 6 kpc in radius (Bik et al. 2024). The inferred $\text{SFR}_{\text{Pa}\alpha} = 205 \pm 15 \text{ Msun yr}^{-1}$ is only a small fraction of the total SFR, which implies a large extinction ($A_V = 17.0$ or $A_{V,\text{mixed}} = 42$; values updated from Bik et al. 2024), even at the wavelength of Pa α $1.876\mu\text{m}$ ($A_{\text{Pa}\alpha} = 2.7$). This is also consistent with the non-detection of Pa β (Bik et al. 2024) and the weaker H α and redder continuum in the nucleus compared to the UV-bright region from the NIRSpec MSA PRISM spectrum (Maseda et al. 2024). NIRSpec IFU observations of H α (Übler et al. 2024) show emission extended over 15 kpc, peaking in the UV-bright region to the north-west. The large-scale ionised gas kinematics are consistent with a turbulent, rotating disk, as seen in the molecular gas (Hodge et al. 2012). There are some indications that GN20 may host an AGN: there is weaker, broad H α emission detected in the center, coinciding with the peak of the stellar emission, that could indicate high-velocity outflows or a broad-line region around an AGN, as well as an elevated [N II]/H α $\lambda 6565$ ratio (Übler et al. 2024). PAH emission was detected at $6.2\mu\text{m}$ with Spitzer, consistent with the large SFR, with the underlying dust continuum consistent with being powered by a starburst and potentially a faint, dust-obscured and Compton-thick AGN, that may contribute up to $\sim 15\%$ of the infrared luminosity, but remains undetected in deep X-ray observations (Riechers et al. 2014). Cortzen et al. (2020) argued that the far-IR dust emission is best described with a dust SED becoming optically thick at $\lambda_0 = 170 \pm 23\mu\text{m}$, yielding a dust temperature of $52 \pm 5\text{ K}$, close to the excitation temperature ($48 \pm 12\text{ K}$) of the optically thin [C II] $609, 370\mu\text{m}$ lines. GN20 is difficult to observe in [C II] $158\mu\text{m}$ due to poor atmospheric transmission at 376 GHz, but was recently detected in [N II] $205\mu\text{m}$ (Kolupuri et al. 2025).

In this paper, we present new sensitive and high-resolution $0.^{\prime\prime}13 - 0.^{\prime\prime}23$ ($0.9 - 1.6\text{ kpc}$) NOEMA imaging of the 1.1 mm (rest-frame $220\mu\text{m}$) dust emission of GN20. We compare this to JWST/NIRCam, NIRSpec and MIRI imaging and spectroscopy, that now detects and resolves the stellar and ionized gas emission, as well as the existing JVLA $^{12}\text{CO}(2-1)$ and PdBI $880\mu\text{m}$ dust continuum imaging. The observations are presented in § 2. In § 3, we show that dust is detected over the full stellar and molecular gas disk of GN20, albeit with a more concentrated light distribution. In

§ 4, we perform self-consistent radiative transfer modeling of the integrated CO and dust continuum emission to measure the gas and dust mass of the system. We then model the integrated emission together with the resolved CO and dust emission. We show that the distinct observed profiles are in fact consistent with a single gas and dust distribution throughout the starburst and can be explained simply due to radiative transfer effects. The implications of these results for comparing observed gas and dust profiles and sizes are discussed in § 5. The extended dust in GN20 implies a lower dust optical depth than previously reported by Cortzen et al. (2020). Finally, we discuss the mounting evidence that GN20 experienced a recent interaction or merger that likely invigorated the starburst. Throughout this paper, we adopt a Planck Collaboration et al. (2020) cosmology (flat Λ CDM with $H_0 = 67.66 \text{ km s}^{-1} \text{ Mpc}^{-1}$, $\Omega_m = 0.3111$ and $\Omega_\Lambda = 0.6889$). At the redshift of GN20 ($z = 4.055$) $1''0$ corresponds to a proper distance of 7.07 kpc. We use log to denote \log_{10} and ln for the natural logarithm.

2. OBSERVATIONS AND DATA REDUCTION

2.1. NOEMA 1.1 mm

GN20 was observed with NOEMA in A configuration using all 12 antennas with the longest baselines up to 1.7 km. The band 3 receivers were tuned to 261 GHz (1.1 mm) using the Polyfix correlator with 16 GHz of total bandwidth in the upper and lower sideband. Four tracks of varying length were obtained during the winter semester of 2023, on February 21st and 23rd and March 1st and 4–5th. The first three tracks suffered from poor observing conditions and high phase rms, but the final track was taken under good conditions and provided a total of 2.3 h of on-source data. Given the limited *uv*-coverage of this single track and the thus asymmetric beam, two additional tracks were observed in A configuration during the winter of 2024 on February 17th and March 7th. The former track again suffered from poor observing conditions, while the final track was taken under better weather and provided 2.6 h of on-source time with orthogonal *uv*-coverage. In addition to the A configuration data, a 2.2 h track in C configuration was observed on April 19–20th, 2023 to fill in short spacings.

The data reduction and imaging were performed at IRAM using GILDAS¹. The bandpass calibrators were 3C273 (March 4 and April 19) and 3C279 (March 7) and the flux calibrators were J2010+723 (March 4) and MWC349 (April 19 and March 7). J1125+596 and J1302+690 were used as amplitude and phase calibrators on all tracks (using average polarisation mode, as both sources are polarised). We inspect the cubes for parasites and ranges with elevated rms and mask channels

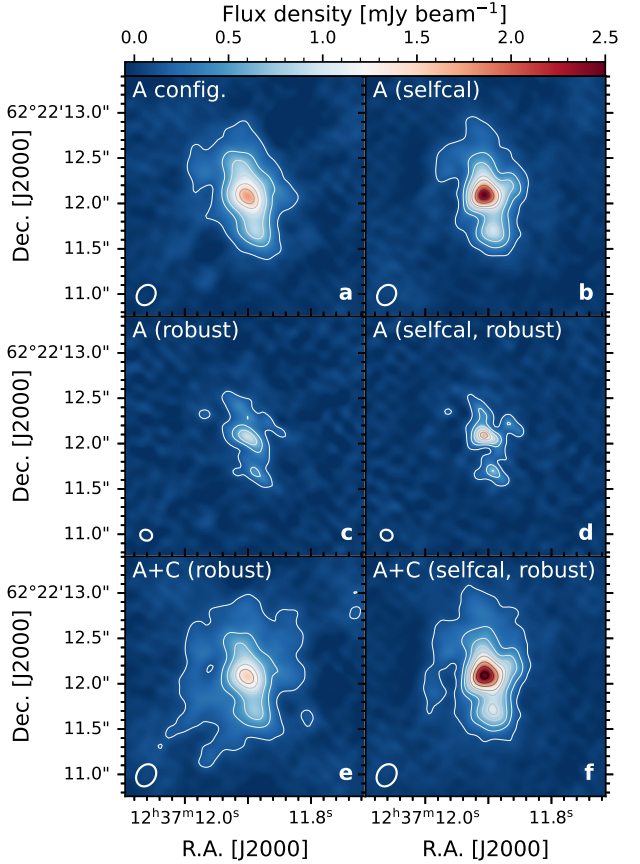


Figure 1. IRAM/NOEMA long-baseline 1.1 mm imaging of GN20. The left and right columns show the cleaned images before and after self calibration. The panels show the (a) highest resolution A-configuration tracks only, at natural resolution ($0''.24 \times 0''.2$), before and (b) after self calibration, (c) A tracks, robust weighted to higher resolution ($0''.14 \times 0''.12$), before and (d) after self calibration, (e) A+C configuration tracks, robust weighted to the A configuration-only resolution ($0''.26 \times 0''.2$) before and (f) after self-calibration. Contours are overlaid on all images, starting at 5σ increasing in steps of 10σ up to 55σ and then steps of 20σ .

accordingly. We then combine the sidebands adopting the measured continuum spectral index between the sidebands of -3.5.

We imaged both the A tracks individually, providing the highest resolution data, as well as the combination of the A and C tracks. Only the two good A configuration tracks were used in the end, as we found that adding in the additional, low quality, A configuration tracks did not impact the final images given the low weight of the visibilities.

We clean the maps down to their 1σ noise level using an elliptical $2''.2 \times 1''.7$ mask centered on the source at a matching position angle using the HOGBOM algorithm (using multi-scale clean instead yields essentially the same map). The synthesized beam of the naturally weighted image using just the A tracks is $0''.25 \times 0''.2$. We also apply robust weighting

¹ <http://www.iram.fr/IRAMFR/GILDAS>

to obtain a map at very high ($0.^{\prime\prime}14 \times 0.^{\prime\prime}12$) resolution, highlighting the small-scale structure. Both images are shown in Fig. 1.

As the cleaned images still show structure in the residuals that could indicate poor phase solutions, we subsequently self-calibrate the data. We use three iterations of phase self calibration with integration times of 135, 90 and 45 seconds (the time per scan is 22 seconds), increasing the number of clean components to build the source model as 50, 100, 150, using the same clean mask. The number of clean components is motivated by the number required to describe the source structure without introducing negative clean components. We let the minimum signal-to-noise ratio for a visibility to be self-calibrated be 3 and keep the baselines that cannot be self-calibrated. We experimented with varying the averaging times, number of clean components and the size of the clean support within reasonable limits, and found that this has limited impact on the final result, yielding qualitatively the same map.

We perform the same procedure for the combined A+C configuration data. The root-mean-square noise in the map is $23 \mu\text{Jy beam}^{-1}$ (for comparison, the theoretically expected rms is $21.8 \mu\text{Jy beam}^{-1}$). As the naturally weighted beam for the combined data is larger ($0.^{\prime\prime}35 \times 0.^{\prime\prime}3$), we apply robust weighting to achieve approximately the same resolution as the A configuration data for the final map. The self-calibrated maps are shown in Fig. 1. The beam size of the final map is $0.^{\prime\prime}26 \times 0.^{\prime\prime}2$ corresponding to a physical resolution of $1.77 \times 1.41 \text{ kpc}$, with an rms noise of $21.5 \mu\text{Jy beam}^{-1}$.

Comparing total fluxes in the maps in Fig. 1 row by row, we find roughly 10.0, 9.0 and 11.5 mJy, with similar results before and after selfcal. This implies most of the flux is already recovered in the A-configuration map alone, with the high-resolution map missing a larger fraction of the extended flux, while the final map including the low-resolution C-config data recovers all the flux (see § 3).

2.2. Ancillary resolved data

The dust continuum at $880 \mu\text{m}$ (rest-frame $175 \mu\text{m}$) was obtained with the Plateau de Bure Interferometer and presented in Hodge et al. (2015). These data have a synthesized beam of $0.^{\prime\prime}3 \times 0.^{\prime\prime}2$, PA= 37° and an rms of $0.25 \text{ mJy beam}^{-1}$ (about $10\times$ higher than the NOEMA data presented here).

The $^{12}\text{CO}(2-1)$ imaging (hereafter CO) was obtained with the Jansky Very Large Array at 45 GHz and we use the moment 0 map presented by Hodge et al. (2012), with a synthesized beam size $0.^{\prime\prime}19 \times 0.^{\prime\prime}17$.

JWST/MIRI and NIRCam imaging of GN20 were taken as part of program ID 1264 (PI: Luis Colina). The MIRI/F560W imaging of GN20, tracing the rest-frame $\sim 1 \mu\text{m}$ stellar emission is presented in Colina et al. (2023). The data processing of the complete MIRI imaging of GN20 and known mem-

bers of the protocluster (in F560W, F770W, F1280W and F1800W) is presented in Crespo Gómez et al. (2024). For NIRCam, F200W and F356W imaging with 1825.3s of integration time were distributed in five dithers, each with one integration, using seven groups with the SHALLOW4 readout mode. Imaging in F115W, F150W, F277W and F444W used the same readout configuration for a total time of 2555.4 seconds distributed in seven dithers. The NIRCam data was calibrated using a custom procedure built on the JWST calibration pipeline (v1.12.3) with CRDS context 1145. The process includes the removal of snowballs and wisps following Bagley et al. (2023), and a superbackground homogenization with 1/f correction as described by Pérez-González et al. (2023). The final mosaics were resampled to a uniform pixel scale of $0.03 \text{ arcsec/pixel}$.

The JWST/MIRI MRS map of $\text{Pa}\alpha 1.876 \mu\text{m}$ is presented in Bik et al. (2024). The $\text{H}\alpha \lambda 6565$ map from the JWST/NIRSpec IFU is presented in Übler et al. (2024).

A JWST/NIRCam color image of GN20 is shown in comparison to the new NOEMA data in Fig. 2. Multi-wavelength cutouts are shown in Fig. 3.

3. ANALYSIS AND RESULTS

3.1. Dust emission at rest-frame $220 \mu\text{m}$

The dust emission from GN20 at 1.1 mm (rest-frame 220 micron) is well resolved and extended, and detected out to the same radius as the rest-frame $1-2 \mu\text{m}$ stellar emission (traced by MIRI) and the molecular gas emission (traced by CO). The total dust emitting region spans an elliptical region of around $13.8 \times 10.3 \text{ kpc}$ ($1.^{\prime\prime}95 \times 1.^{\prime\prime}45$) at 3σ , or $12.4 \times 8.8 \text{ kpc}$ ($1.^{\prime\prime}75 \times 1.^{\prime\prime}25$) at 5σ .

The total flux in the final map is $f_{\nu, 1.1 \text{ mm}} = 11.45 \pm 0.23 \text{ mJy}$, which is consistent with the total flux from the C-configuration track and the flux measured at 1.1 mm by AzTEC at the JCMT of $11.45 \pm 0.99 \text{ mJy}$ (Perera et al. 2008).

The 1.1 mm dust emission extends asymmetrically around the nucleus in the north-south direction. A significant clump is detected towards the south, and extended emission is also seen to the east. The highest resolution map reveals several fainter peaks in the dust emission at these locations (see Fig. 1), implying a clumpy structure in the dust on these scales. On larger scales, there is fainter emission extending in all directions, but in particular towards the north, over the full extent of the stellar and molecular gas in GN20 (Fig. 3).

Of the total flux, $\approx 2.6 \text{ mJy}$ is contained in the central point source at (23%) and $\approx 1.0 \text{ mJy}$ in the southern point source (9%). The total flux contained in the brightest central region of $\approx 0.^{\prime\prime}5 \times 0.^{\prime\prime}2$ along the major axis of the source is $\approx 7 \text{ mJy}$ (measured as the flux with in the 20σ contour) indicating that a significant fraction of the total emission is coming from large radii.

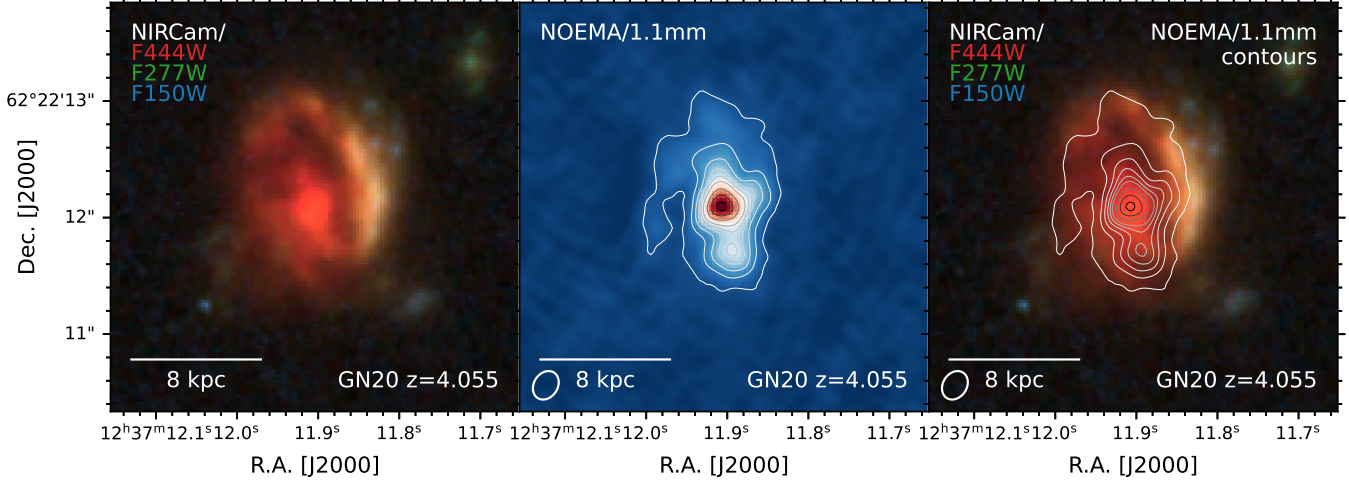


Figure 2. JWST/NIRCam and NOEMA 1.1 mm imaging ($4' \times 4'$ cutouts) of GN20 at $z = 4.055$. Dust contours start at 5σ and increase in steps of 10σ up to 55σ and then steps of 20σ up to 115σ .

While the continuum morphology of GN20 is complex, to quantify the overall extent of the 1.1 mm dust emission and facilitate a comparison to other work, we fit a two-dimensional Gaussian as well as a Sérsic (1968) profile to the cleaned image using GALFIT (Peng et al. 2002). We use the Gaussian synthesized beam model as kernel to obtain ‘deconvolved’ size measurements. The best-fit Gaussian model yields a FWHM of the major axis of $0''.64 \pm 0''.01$ (4.53 ± 0.02 kpc) with a $b/a = 0.488 \pm 0.003$. We fit both a model with free Sérsic index n , as well as a model with $n = 1$. The former provides a best-fit for $n = 2.01 \pm 0.03$, with an effective radius of 3.18 ± 0.04 kpc ($0''.45$) and axis ratio $b/a = 0.458 \pm 0.004$. Similar results are obtained for the $n = 1$ fit, with $r_e = 2.48 \pm 0.02$ kpc ($0''.35$) and $b/a = 0.501 \pm 0.003$. Note that the uncertainties are typically underestimated by GALFIT (see van der Wel et al. 2012). Overall we conclude that $r_e(1.1 \text{ mm}) \approx 2.5$ kpc ($0''.35$ – $0''.4$) with an axis ratio $b/a \approx 0.5$.

3.2. Comparison to multi-wavelength data

A multi-wavelength overview of GN20 is shown in Fig. 3. The bulk of the dust emission is coming from the region that is completely obscured in bands bluer than F277W (rest-frame $0.55 \mu\text{m}$), and extends up to the edge of the UV-bright region in the west. This is consistent with dust obscuring most of the galaxy in the rest-frame UV/optical. The dust emission peaks at R.A.= $12^{\text{h}}37^{\text{m}}11^{\text{s}}906$, Decl.= $+62^{\circ}22'12''091$. The peak is co-spatial with the peak of the stellar emission at rest-frame $1.1 \mu\text{m}$ (traced by MIRI) and the molecular gas emission (traced by CO), and has a similar extent.

The NIRCam imaging now clearly reveals the morphology of the arm-like feature that loops around the western part of the galaxy from the south to north, of which the least-obscured part coincides with the UV/optical-bright part of the galaxy.

The ‘gap’ in the stellar emission between the nucleus and arm to the north-west already seen in MIRI aligns with a drop in the dust emission, suggesting this is a real gap in the stellar distribution separating a spiral arm or tidal feature, rather than being caused by spatially varying extinction. The clump in the dust emission to the south is coincident with one of the clumps identified in the $1.1 \mu\text{m}$ residual image by Colina et al. (2023) (cf. Crespo Gómez et al. 2024).

The north-south bar feature in the dust emission matches that seen at $880 \mu\text{m}$ (Hodge et al. 2015). A similar structure is now also seen in the rest-frame near-infrared stellar morphology around ~ 1 – $1.5 \mu\text{m}$ and indicates the presence of a stellar bar in GN20. The 1.1 mm-clump in the south then roughly coincides with enhanced star formation at the tip of the bar. A detailed study of the stellar bar will be presented in a forthcoming paper. Note most of the smaller-scale clumps and structural details seen at 1.1 mm are not visible in the early (6 antenna) PdBI map at $880 \mu\text{m}$, likely because of the $10\times$ higher rms noise.

The central region that is brightest in dust continuum emission is largely co-spatial with the region brightest in CO and the peak of the dust emission is close to the peak of the CO emission. The dust clump to the south is not co-spatial with, but rather in-between, the CO clumps identified by Hodge et al. (2012, indicated on Fig. 3). Interestingly, the Pa α emission (Bik et al. 2024) seems to avoid the regions that have the highest dust intensity, in particular the bright clump in dust emission towards the south, instead being brightest in the north-east where the dust emission is fainter and more extended. The Pa α peak in the center is co-spatial with the dust emission. A similar picture is seen in H α (Übler et al. 2024). While there does not need to be one-to-one correspondence between the extinguishing and emitting dust, this picture is consistent with higher extinction in those regions.

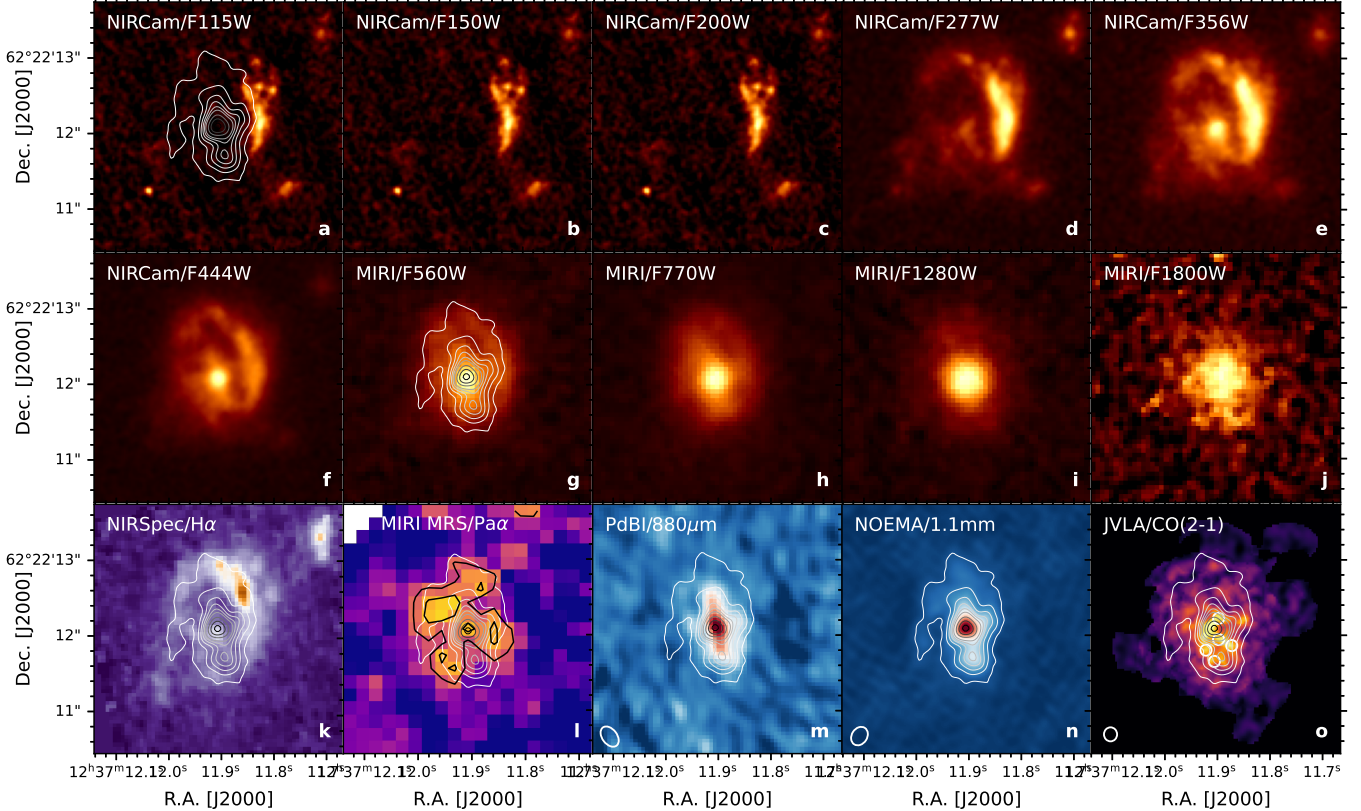


Figure 3. Multi-wavelength cutouts of GN20. The top two rows show the NIRCam and MIRI imaging (Colina et al. 2023; Crespo Gómez et al. 2024) covering the rest-frame $0.23\text{ }\mu\text{m}$ – $3.56\text{ }\mu\text{m}$ range. The bottom row shows the H α map (Übler et al. 2024), Pa α map (Bik et al. 2024, with 2–3 σ contours overlaid), the dust continuum at $880\text{ }\mu\text{m}$ (PdBI Hodge et al. 2012) and 1.1 mm (NOEMA; this work) and the JVLA/CO(2–1) (Hodge et al. 2012, with their CO clumps indicated). All maps are shown on a linear colorscale and NOEMA contours are overlaid on selected images, starting at 5σ and increasing in steps of 10σ up to 55σ and then steps of 20σ up to 115σ . Beam sizes of the radio maps are shown in the bottom left corner.

3.3. Radial profiles

A false color-image illustrating the spatial distribution of the starlight in the rest-frame UV and near-IR, as well as the dust and gas is shown in Fig. 4. To study the spatial distribution of the stellar, dust and gas emission, we compute azimuthally averaged radial profiles using PHOTUTILS, propagating errors. We use circular profiles, to facilitate a comparison given the different axis-ratios between the dust, stars and gas in GN20; with a lower ellipticity in the stellar emission, and similar or even lower for the gas. The resulting profiles are shown in Fig. 5.

Notably, the rest-frame near-IR stellar emission and the molecular gas follow each other closely, at all radii. In contrast, the dust emission both at 1.1 mm (rest-frame $220\text{ }\mu\text{m}$) and (at lower S/N) $880\text{ }\mu\text{m}$ (rest-frame $175\text{ }\mu\text{m}$), shows a significantly more concentrated distribution. This is consistent with the two-dimensional Sérsic fits, that yield a smaller effective radius for the dust ($r_{e,220\text{ }\mu\text{m}} \approx 2.5\text{ kpc}$) compared to the stellar disk ($r_{e,1.1\text{ }\mu\text{m}} = 3.6\text{ kpc}$; Colina et al. 2023). The rest-frame UV emission instead is offset with a peak around 4 kpc and little emission from the center. Note that due to the

asymmetric dust emission and circular apertures, more dust emission appears to come from the UV-bright region than is actually the case (cf. Fig. 3).

4. RADIATIVE TRANSFER MODELING

A key question that arises from Fig. 4 and Fig. 5 is whether the distinct radial profiles of the gas and the dust imply that the gas and dust have intrinsically different spatial distributions, or whether they could also arise from gas and dust with the same spatial distribution, with the observed different profiles being driven by radiative transfer effects (e.g., Calistro Rivera et al. 2018).

To investigate this, and also to derive the molecular gas and dust masses and properties of GN20, we model the CO and the dust continuum emission using a radiative transfer model that we call TUNER (Turbulent Non-Equilibrium Radiative Transfer). TUNER uses a physically-motivated (log-normal) density and density-coupled temperature distribution, together with the Large Velocity Gradient (LVG) and escape probability approximations, to solve for both the line and continuum opacities of the molecular ISM simultane-

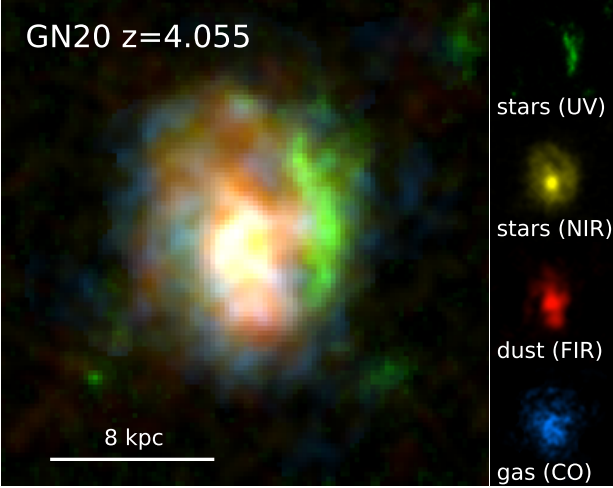


Figure 4. $3'' \times 3''$ false color image of GN20 at $z = 4.055$ highlighting the distinct spatial distribution of the different components: rest-frame UV (NIRCam/F150W), rest-frame near-IR (MIRI F560W, yellow), rest-frame $220\text{ }\mu\text{m}$ dust continuum (NOEMA/1.1mm) and the molecular gas traced by CO(2–1) (VLA). The stellar distribution traced by the rest-frame near-IR is largely cospatial with the CO and the dust emission, though the emission from the latter appears more centrally concentrated. The (unattenuated) rest-frame UV light is only visible in the outskirts.

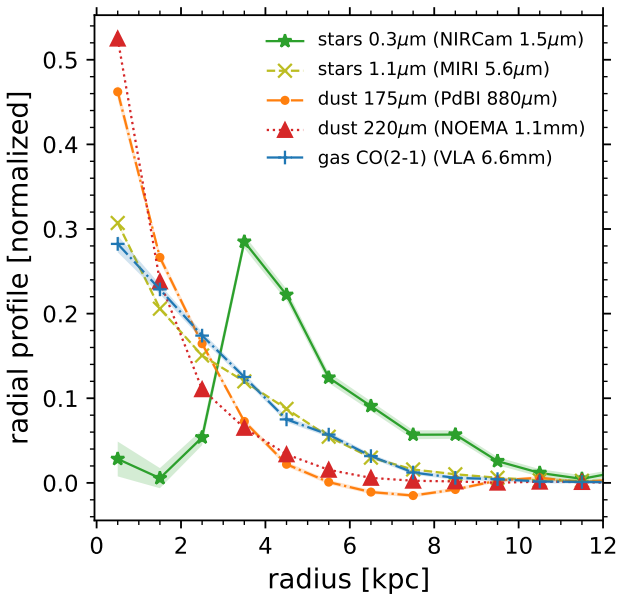


Figure 5. Azimuthally averaged and integral-normalized radial profiles, measured from the peak of the NOEMA continuum emission in bins of 1 kpc.

ously and self-consistently. The details of the TUNER model are explained in more detail in Appendix A.

We first use TUNER to model the integrated (unresolved) CO and dust continuum SED of GN20 in § 4.1. We then

couple individual TUNER models to a Sérsic profile and a radial temperature distribution to study the resolved CO and dust profiles of GN20 in § 4.2. The new and existing far-infrared photometry and line-flux measurements for GN20 are compiled in Table 1.

4.1. Integrated CO and dust SED

The integrated CO and dust continuum emission from GN20 is shown in Fig. 6. For the CO(2–1) flux of GN20, we adopt the lowest-resolution integrated flux measurement from Carilli et al. (2010), which is lower than that from Carilli et al. (2011) and Hodge et al. (2012), though consistent within error, but best-agrees with the results from the radiative transfer modeling, as discussed below.

For the TUNER modelling, we adopt uniform priors on the parameters with the following bounds: radius $\in [0.1, 10^4]\text{ pc}$, $n_{\text{H}_2} \in [1, 10^7]\text{ cm}^{-3}$, $T_{\text{kin}} \in [10, 600]\text{ K}$, a temperature power law slope as function of density $\gamma_T \in [-0.5, 0.05]$, abundance $[\text{CO}/\text{H}_2] \in [10^{-6}, 10^{-3}]$, gas-to-dust ratio $\delta_{\text{GDR}} \in [1, 250]$, dust opacity slope $\beta \in [1.2, 3.6]$. The prior on the dust temperature is coupled to the T_{kin} such that $T_{\text{kin}}/T_{\text{dust}} \in [0.5, 6.0]$. We assume a virial parameter $\kappa_{\text{vir}} = 1$ and a dust opacity of $\kappa_0 = 0.47\text{ cm}^2\text{ g}^{-1}$ at $\nu_0 = 352.7\text{ GHz}$ (Draine et al. 2014).

A key parameter is the turbulent velocity width of the lognormal distribution, Δv_{turb} , which turns out to be poorly constrained in the unresolved modeling of GN20 (likely because of the lack of high-density tracers), and asymptotes to high Δv_{turb} values ($\gg 100\text{ km s}^{-1}$), with a weak local minimum around $\sim 20\text{--}40\text{ km s}^{-1}$. While these broad distributions provide equally good fits, but may have unrealistically large masses, because they can hide a lot of material at high density and low temperature where it emits very little. We therefore constrain the turbulent width in the model using the resolved spectroscopic data. Hodge et al. (2012) measured the width of individual CO clumps in the disk to be $90\text{--}150\text{ km s}^{-1}$, with the central and highest-S/N clump having a $\text{FWHM} = 90 \pm 40\text{ km s}^{-1}$ (after rotation and beam-smearing corrections). Given the beam size, these line widths are still upper limits on the actual velocity dispersion in the gas. For the ionized gas, which typically has a dispersion of a factor 2–3× larger than the cold gas (Girard et al. 2021; Rizzo et al. 2024), Bik et al. (2024) find a dispersion of $40\text{--}140\text{ km s}^{-1}$ in $\text{Pa}\alpha$, while Übler et al. (2024) find $90 \pm 10\text{ km s}^{-1}$ for $\text{H}\alpha$. From the resolved modeling (see § 4.2) we consistently find Δv_{turb} in the range of $20\text{--}65\text{ km s}^{-1}$, with a best-fit value around 30 km s^{-1} . We therefore fix $\Delta v_{\text{turb}} = 30\text{ km s}^{-1}$, but also perform two runs with 90 and 10 km s^{-1} (smaller values Δv_{turb} require unrealistically large radii of $> 10\text{ kpc}$ to match the observed fluxes), finding consistent results.

The best fit is shown in Fig. 6 and the full posterior in Fig. 10 in Appendix B. Overall, the model provides a very good description of the unresolved CO and dust SED of GN20. To

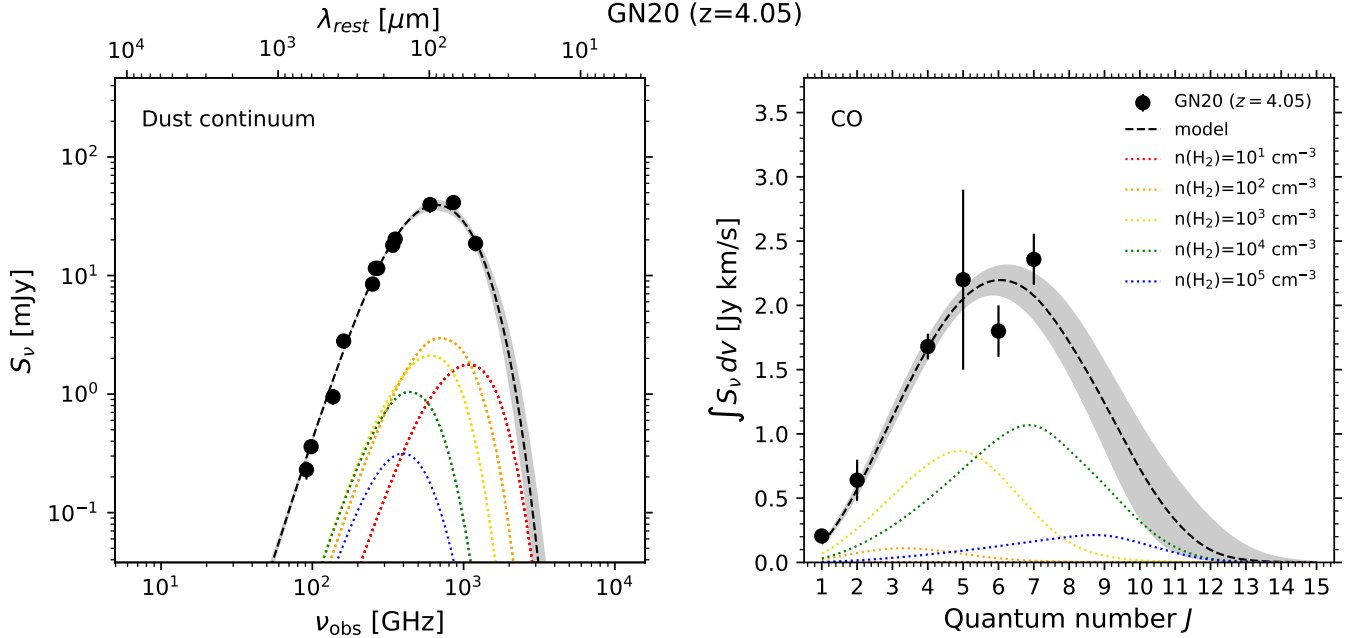


Figure 6. Best-fit TUNER model for the integrated (unresolved) GN20 data. The black points show the observations, the dashed line with gray band the median model with $\pm 1\sigma$ percentiles. The colored lines highlight the contributions of a few individual density components (scaled up for visibility). Overall the model provides a very good simultaneous fit to the dust continuum and CO data.

show how the emission of different density components in the model contributes to the overall SEDs, we highlight a subset of the components (by powers of 10, scaled up for clarity). The dominant contributions to the CO ladder come from H₂ gas at densities around 10^3 and 10^4 cm⁻³. Note there is observational tension between the CO(6–5) and CO(7–6) measurements which cannot both be fit by the model simultaneously. This is most likely a limitation of the data, as it is difficult to imagine a physical scenario in which the CO ladder has a sudden ‘dip’ at the CO(6–5) transition, unless there is an additional component that strongly picks up in the high- J lines. Note if we remove either transition from the data we can provide an excellent fit to the remaining data points, with little impact on the total mass or conclusions of the paper. Future observations of higher- J lines could shed light on this.

From the unresolved model, we derive a total molecular gas mass of $M_{\text{mol}} = 3.4^{+5.9}_{-1.8} \times 10^{11} M_{\odot}$, with an $\alpha_{\text{CO}} = 3.6^{+7.3}_{-1.4}$, higher than the dynamically constrained limit from 1.1 ± 0.6 from (Hodge et al. 2012, though consistent within substantial errors). The larger upward errors are partly driven by the high turbulent velocity width, that implies a significant fraction of high-density gas that is hard to constrain with the unresolved ¹²CO data alone, though we refer to § 4.2 for more precise constraints when including resolved data (in good agreement with the median values).

At face value the molecular gas mass estimate is higher than the gas mass estimate from the single CO(1–0) line of $1.3 \pm 0.4 \times 10^{11} (\alpha_{\text{CO}}/0.8) M_{\odot}$ (Carilli et al. 2010), though it

is slightly lower after accounting for the difference in conversion factors, as the model predicts a slightly lower CO(1–0) flux. Earlier single- and two-component LVG modelling by Carilli et al. (2010) noted that the CO(1–0) flux could not be described by a single gas component (underpredicting the flux by a factor $\geq 2\times$) and required a second, more extended, low density component (it should be noted that these two component models are highly degenerate and strong assumptions are required on the sizes of these components; cf. Daddi et al. 2015). We now find much better agreement using the turbulent gas distribution (with fewer free parameters), but note that the measured CO(1–0) flux from Carilli et al. (2010) is still underpredicted by $\sim 30\text{--}50\%$ (at 1.5σ significance). While this could simply be the result of the measurement error, in particular on the faint low- J CO lines, given the good overall agreement for the higher- J lines, together with the potentially higher CO(2–1) flux, this could also imply the presence of an additional gas component with a significantly distinct spatial distribution (such as a low-density component with a much larger extent radius than that occupied by the higher-density gas), such that it cannot be captured through a single log-normal distribution. This kind of distinct two-component (turbulence) modeling is significantly more degenerate and thus requires additional assumptions which we leave to future work. Instead, we focus on modeling the resolved profiles together with the integrated values in the next section § 4.2. Still, to test the impact on the gas-mass estimate of a potential low-density, low-excitation component, however, we run an

additional model using a significantly higher CO(2–1) flux of $1.0 \pm 0.3 \text{ Jy km s}^{-1}$ (cf. Hodge et al. 2012), to see if this results in a model with higher low- J line luminosities. It does not. Instead, it hardly produces a better fit to the CO(1–0) data and a poor fit the $J_{\text{up}} = 2$ line, while the total gas mass estimates remain consistent with the fiducial model.

The estimated total molecular gas mass implies that GN20 is predominantly gas rich, with the molecular gas mass exceeding the estimated stellar mass ($\approx 10^{11} M_{\odot}$) and comprising the majority of the total (dynamical) mass of $M_{\text{dyn}} \approx 5 \times 10^{11} M_{\odot}$ (Hodge et al. 2012; Übler et al. 2024).

Turning to the dust, we measure an $L_{\text{IR}} = 1.6_{-0.1}^{+0.1} \times 10^{13} L_{\odot}$, in perfect agreement with general opacity model from (Cortzen et al. 2020). An interesting result from the self-consistent modeling is that the gas-to-dust ratio, δ_{GDR} , is quite low, with a median posterior value of ≈ 50 (about 3x lower than the typical ISM value), while the median $[\text{CO}/\text{H}_2] \approx 10^{-4}$ is closer to the typical abundance of CO in the ISM (Frerking et al. 1982; Sofia et al. 2004; Lacy et al. 2017). We note that $[\text{CO}/\text{H}_2]$ runs into the upper bound of the prior (set at $\log([\text{CO}/\text{H}_2]) = -3.0$), which may impact the median posterior value. We argue this is not an issue, given that the upper bound is physically motivated, being about 5x higher than the highest abundance measured in the Milky Way (Sofia et al. 2004; Lacy et al. 2017). Indeed, taking the carbon abundance from Asplund et al. (2009), assuming most hydrogen is in H_2 at the molecular cloud densities of the model, and furthermore assuming that all carbon is locked in CO, would result in $\log([\text{CO}/\text{H}_2]) = -3.3$. The latter assumption is certainly a strong overestimation given that a significant fraction of the carbon will be locked in dust grains (as said, the measured value in the solar neighborhood is closer to -4.0) and thus especially for GN20, given its significant dust mass. Under these assumptions, the adopted bound of -3.0 corresponds to taking about twice the Asplund et al. (2009) abundance (i.e., further assuming that GN20 has $\sim 2\times$ solar metallicity).

The relatively small G/D ratio implies a relatively large fraction of mass in dust grains, as may be expected in denser environments (e.g., Patra et al. 2025). Alternatively, if the true δ_{GDR} is actually solar (i.e., 100–150), given that the δ_{GDR} is inversely proportional to the dust opacity (at fixed dust mass), it would imply that the dust opacity in GN20 is $\sim 2\text{--}3\times$ larger than the adopted value from Draine et al. (2014). Such opacity would be higher even than the dust opacity from (Dunne et al. 2000, used by e.g., Da Cunha et al. 2015), which is a factor $1.8\times$ higher than the Draine et al. (2014) value. The median posterior $\beta \sim 2.2$ is higher than the commonly assumed value of 1.8, yet closer to the value of 2.08 from Draine et al. (2014). The total derived dust mass is $M_{\text{dust}} = 5.9_{-1.0}^{+0.6} \times 10^9 M_{\odot}$, higher than the estimate of $2.0 \pm 0.8 \times 10^9$ for optically thick dust from Cortzen et al. (2020), consistent with the lower

δ_{GDR} . Note that rescaling the dust opacity in the model does not impact the derived (dust) mass, as the δ_{GDR} compensates accordingly (but consistent dust opacities and β 's should be used when comparing mass estimates from different sources). It should be noted the CO abundance and δ_{GDR} do not directly couple and are non-linearly dependent on the gas conditions and metallicities (Sandstrom et al. 2013; Rémy-Ruyer et al. 2014). As such, the discrepancy between the δ_{GDR} and the $[\text{CO}/\text{H}_2]$ does not necessarily imply that the dust opacity is different. A different dust opacity could point to significantly different properties of the dust in GN20. Given the extreme gas densities and conditions in the dusty starburst galaxy, this may not be surprising.

4.2. Resolved CO and dust profiles

We model the resolved radial profiles of the CO and dust continuum by combining individual TUNER models to build a spatially resolved profile. We call this combination of TUNER models the TED model (Turbulent Extended Distribution). *Critically*, we take a constant $[\text{CO}/\text{H}_2]$ and δ_{GDR} throughout the entire profile, such that the gas and dust follow the same intrinsic radial distribution. We assume the gas column density follows a Sérsic (1963) profile with a linear radial kinetic- and dust temperature gradient (dT/dr). We divide the profile into annuli and at each radius compute a TUNER model for the corresponding solid angle of the annulus and mean density and temperatures. The density and temperature parameters are taken to be the values in the center. The resulting model fluxes of each ring are both summed to yield total fluxes, to be fit to the unresolved data, as well as combined into a radial profile and convolved by the beam of the respective observations, to be fit the observed profiles. The model is computed outward in radial bins in steps that ensure sufficient resolution in density and temperature until the flux in the CO ground state is converged to within 1%. We model the observed profiles out to a radius of 8 kpc. Specific care needs to be taken to ensure consistency between the unresolved and resolved flux measurements. While the total fluxes from the resolved and integrated observations are generally consistent within error (cf. Hodge et al. 2015), absolute differences will lead to inconsistencies in the modelling, where the profiles by construction integrate to the total flux. To ensure consistency, we adopt a 20% calibration uncertainty, an error floor on the error beyond the effective radius, and renormalize the resolved CO(2–1) and PdBI 850 μm profiles such that they integrate to their unresolved integrated flux measurements (mainly relevant for the CO map).

We adopt uniform priors on the scale radius $r_{\text{exp}} \in [500, 6000] \text{ pc}$, Sérsic index $n \in [0.5, 4]$, $dT/dr \in [-50, 50] \text{ K kpc}^{-1}$ and model all other parameters with the same priors as in the unresolved modeling (§ 4.1), with two changes: we leave Δv_{turb} free, with a prior of $\Delta v_{\text{turb}} \in [1, 90]$

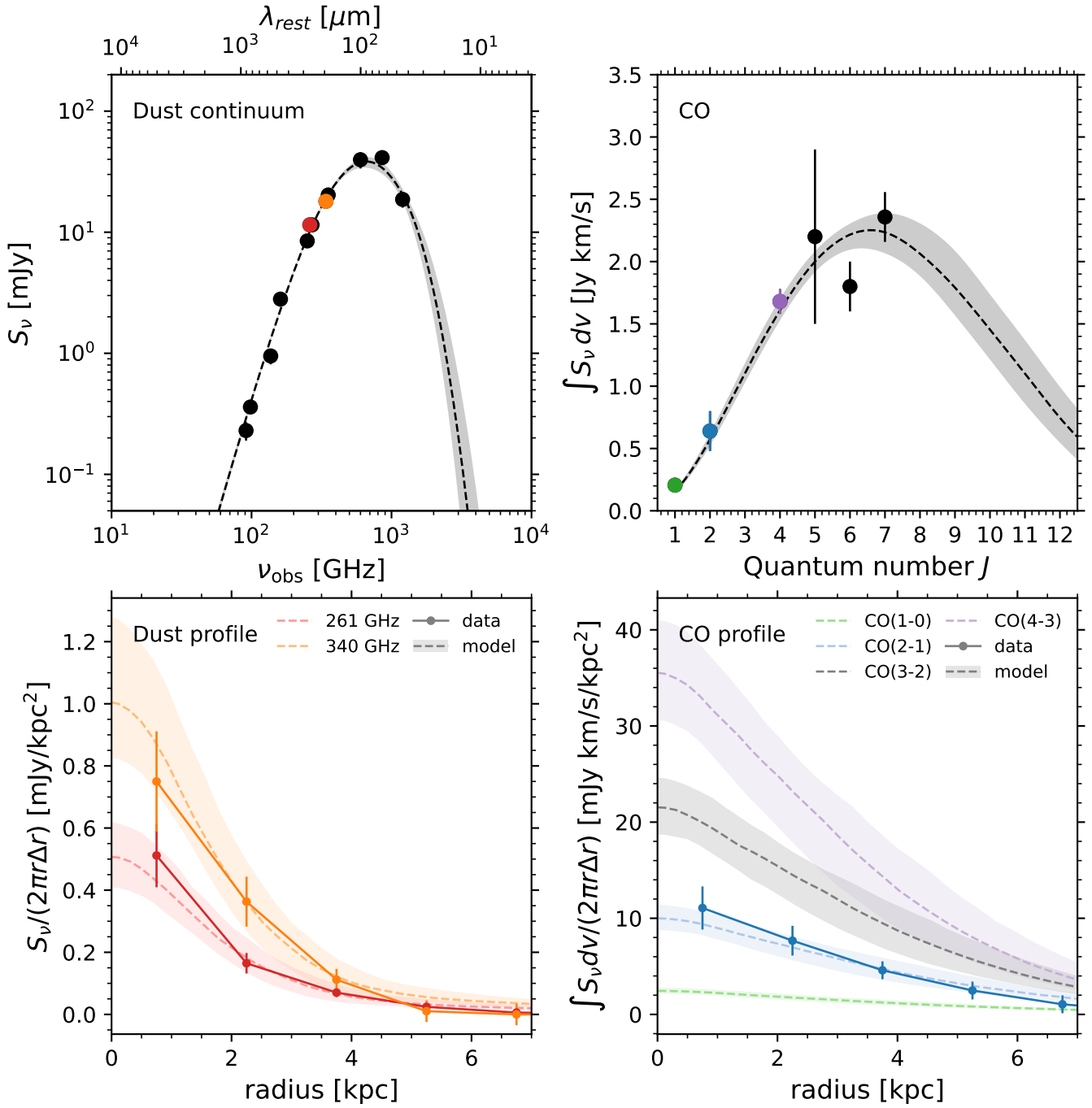


Figure 7. Best-fit TED model for the combined resolved and integrated (unresolved) GN20 data. The top panels show the integrated dust continuum and CO spectral energy distributions, while the bottom panels show the spatially resolved dust and CO radial profiles. The points indicate the data while the dotted line with shading the posterior model. Matching colors are used in the top and bottom panels for dust and CO observations with both integrated and resolved measurements (and their models). The TED radiative transfer model, that is based on a single Sérsic gas mass surface density profile with linear radial temperature gradient and constant CO abundance and gas-to-dust ratio, can provide a good fit to both the resolved and integrated data, implying that the different observed profiles are consistent with a single underlying gas- and dust mass distribution.

(see § 4.1), as we find that it can be well constrained from the TED model. In contrast, we find that leaving the abundances free provides very degenerate constraints with solutions that have several unphysical characteristics (including large gas(-to-dust) masses and conversion factors, that exceed the dynamical constraints by $\geq 10\times$). We therefore fix the abundances to values close to the median best-fit values from the unresolved TUNER model ($\delta_{\text{GDR}} = 50$ and $[\text{CO}/\text{H}_2] = 10^{-4}$). Following the discussion in § 4.1, we also run a model with $[\text{CO}/\text{H}_2] = 10^{-4.3}$ (closer to the posterior peak) and corresponding $\delta_{\text{GDR}} = 65$ (note their non-linear degeneracy in Fig. 10), finding the same results.

The results from the TED model are shown in Fig. 7 and the full posterior in Fig. 11 (Appendix B). What is remarkable is that the model can provide a good simultaneous fit to the radial distributions of CO and the dust continuum, as well as the integrated profiles. We find that for the best-fit model, the intrinsic gas distribution has an $r_{\text{eff,mol}} \approx 4 \text{ kpc}$,² and an $n \approx 1$. The implied $r_{\text{eff,CO}} \approx 4 \text{ kpc}$ is consistent with Hodge et al. (2012), and the $r_{\text{eff,220}\mu\text{m}} \approx 2.5 \text{ kpc}$ is in good agreement with the Sérsic fits (noting the differences in n , see § 3.1). We derive a total molecular gas mass from the TED model of $M_{\text{mol}} = 2.9^{+0.4}_{-0.3} \times 10^{11} \text{ M}_\odot$ with an $\alpha_{\text{CO}} = 2.8^{+0.5}_{-0.3}$. These estimates are very consistent with the estimates from the unresolved data but with smaller error (cf. § 4.1).

A key result of the resolved modeling is that to first order the CO and the dust emission can be described by a single underlying gas density distribution, with a constant CO abundance and δ_{GDR} . This implies the different observed profiles for the dust and CO are not necessarily due to intrinsically different spatial distributions of the gas and dust, but rather due to radiative transfer effects. We further elaborate on this point in § 5.2.

To second order, there are some discrepancies between the model and the observations, most notably that the high-fidelity NOEMA profile at 261 GHz rises more sharply to the center than the earlier PdBI 340 GHz profile. While the model takes into account beam convolution, this cannot be fully described by the model self-consistently under the assumed abundances and temperature gradient, despite the model taking into account optical depth effects. This could also be a limitation of the observations and/or self-calibration, noting that both the PdBI and CO data have significantly lower S/N than the high-fidelity NOEMA observations.

The assumption of a radial temperature gradient is motivated by both theoretical considerations and observations of nearby galaxies (e.g., Galametz et al. 2012; Casasola et al. 2017), and also observed in simulated galaxies (Cochrane

et al. 2019). However, it does not have to be linear and it may be that the true temperature gradient is steeper in the central regions compared to the (outskirts of) the disk. Indeed, we find that the best-fit model prefers a relatively steep gradient, that artificially flattens in the outskirts because the temperatures approach the temperature floor. The relatively steep gradient found in GN20 can therefore be interpreted an average gradient, driven by the central regions. For comparison, we also tested a model without a temperature gradient (fixing $dT/dr = 0$). However, we find this model provides a much poorer fit, as it fails to match both the profile shapes and the integrated fluxes simultaneously.

5. DISCUSSION

5.1. GN20: an extended, interaction-driven starburst

The sensitive NOEMA imaging detects the dust continuum emission out to large radii in GN20 and shows the dust extends over the full extent of the stellar and molecular gas disk. The lower surface brightness dust in the outskirts was not clearly detected in the earlier PdBI observations (Hodge et al. 2015) and emphasizes the importance of sufficient sensitivity when mapping the dust emission in galaxies. About 40% of the total dust luminosity comes from radii outside of the brightest nuclear region, implying that the starburst is very extended, stretching over the entire disk of GN20.

Despite the disk-like ionized- and molecular gas kinematics (Hodge et al. 2012; Bik et al. 2024; Übler et al. 2024), there are several indications that GN20 has undergone a recent interaction or merger. Beyond its location in an overdense protocluster environment (Daddi et al. 2009), these include an offset nucleus and a potentially disturbed morphology with arm or tidal feature in the north (Colina et al. 2023), and the presence of several clumps and nearby companions seen in $\text{H}\alpha \lambda 6565$ emission (Übler et al. 2024). However, as pointed out in those works, these features could also be caused by strongly variable extinction in the dust-rich starburst. The NIRCam and MIRI imaging now reveals more clearly what is an arm or tidal feature to the north. The arm or tidal feature stretches in the direction of the nearby companion that was identified by its $\text{H}\alpha \lambda 6565$ emission (Übler et al. 2024) and is now detected with NIRCam. At the same time, there is no elevated dust emission detected by NOEMA in the ‘gap’ in the stellar emission (rather, the ionized gas maps suggest the extinction is lower in these regions). This implies that the morphological disturbances, including the arm- or tail-like feature, that are seen in the MIRI and long-wavelength NIRCam imaging are likely real and not an effect of extinction. Taken together, these clues provide increasingly strong evidence for the scenario in which GN20 has undergone a recent interaction or merger, that is likely what triggered or enhanced the very intense starburst in the system.

² Note the input radius is not the effective radius, which is instead computed from the gas distribution a posteriori (see Fig. 8).

5.2. Coincident gas and dust throughout the starburst: the importance of accounting for radiative transfer

An important result from the resolved radiative transfer modeling in § 4.2 is that, to first order, the observed radial profiles of the CO and the dust emission can be accurately described using a single underlying gas density distribution with constant [CO/H₂] and δ_{GDR} . This implies that the different observed profiles for the dust and CO are not due to intrinsically different spatial distributions of the gas and dust, but rather due to radiative transfer effects. Such behavior has been suggested before from the average CO and dust continuum profiles in stacked samples of SMGs by Calistro Rivera et al. (2018).

Specifically, the results imply that the smaller ‘size’ of the dust distribution compared to the gas is not due to the dust being actually more concentrated in the center of the galaxy, but can simply be due to radiative transfer. To explain this, we look at the radial profiles of the molecular gas mass surface density, as well as selected CO transitions and the dust at different wavelengths for the best-fit model of GN20 in Fig. 8. We also refer the reader to the equations of radiative transfer given in Appendix A.

In Fig. 8, the molecular gas mass surface distribution is shown by the black line. Looking at the shape of the surface brightness profiles, the low- J CO lines trace the intrinsic shape of the molecular gas surface density profile closely in the outskirts, slightly flattening towards the center, and overall better than the 1.2 mm dust continuum that shows a steeper profile.

This behavior can be explained through radiative transfer as follows: while the low- J CO line emission is optically thick throughout ($\tau_{\nu L} \geq 1$), it is sub-thermally excited in the outskirts ($T_{\text{exc}} < T_{\text{kin}}$). Moving radially inward, the increasing emission is due to the increasing CO excitation as the gas surface density increases, until the CO is both optically thick and thermalized ($T_{\text{exc}} = T_{\text{kin}}$; and thus saturates)³ at which point it can only increase further due to the increasing kinetic temperature (via the radial temperature gradient). In contrast, the (longer-wavelength) dust is optically thin throughout most of the galaxy ($\tau_{\nu, \text{dust}} < 1$), and hence moving radially inward, the emission becomes brighter towards the center both because of the increasing column density (increasing $\tau_{\nu, \text{dust}}$) and the increasing dust temperature T_{dust} , and thus follows a steeper light profile (even if it becomes optically thick in the center). As such, even though the gas and dust share the same underlying mass profile and temperature gradient, the emitted profile for the CO and dust continuum is different.

³ Note it is a misconception that the optically thick ¹²CO emission is not sensitive to the gas mass surface density (or column density); it still is as long as it is subthermally excited, as T_{exc} still increases with higher density (cf. Eq. A2).

From Fig. 8 and the above it also follows that the low- J CO traces the shape of the underlying H₂-mass profile more closely than the mm-continuum, albeit not perfectly if a single conversion factor (and excitation correction for the $J_{\text{up}} > 1$ lines) is used.

It should go without saying that the detailed behavior seen in Fig. 8 is specific to GN20, and variations in this picture are expected for different types of galaxies. However the qualitative behavior of the CO and dust—driven by the former being optically thick in general (at least in the low- J lines) while the latter is optically thin—should hold more generally.

The broader implication is that that careful consideration of radiative transfer effects is important when interpreting observed profiles from gas and dust tracers. A particular example is when comparing gas and dust sizes. Note that while the *observed* effective radii of the CO and dust emission are significantly different, the *intrinsic* effective radii of the gas and dust distributions in the model are exactly the same. A face-to-face comparison of the effective radii or other measures of the observed profiles between different gas and dust emission to measure their size or extent is therefore misleading.

5.3. Deceptively optically thick dust in GN20?

The median dust optical depths predicted from the TED model are shown in Fig. 9. The dust is globally optically thin at wavelengths longer than $\approx 100 \mu\text{m}$. At the effective radius, the wavelength where the dust becomes optically thick is $\approx 70 \mu\text{m}$, very consistent with average value of $\approx 70 \mu\text{m}$ from the unresolved TUNER model.⁴

The dust optical depths from the model are significantly lower than previously reported by Cortzen et al. (2020), found that the global wavelength where the dust gets optically thick is $170 \pm 23 \mu\text{m}$ (for a very similar dust opacity of $0.43 \text{ cm}^2 \text{ g}^{-1}$ from Li & Draine 2001) resulting in a higher T_{dust} . The high optical depth found in Cortzen et al. (2020) corresponds to an radius of $\approx 1.2 \text{ kpc}$, which they noted to be broadly consistent with the effective radius of the PdBI data from Hodge et al. (2015). Looking in detail, however, the deconvolved FWHM size measured by (Hodge et al. 2015) in fact corresponds to a radius of $\approx 2 \text{ kpc}$ (which can also be read-off directly from Fig. 5). This implies that the actual dust column is lower and the wavelength where the dust is optically thick (using their values) comes closer to ~ 100 micron. Note that there is no physical mechanism that requires $T_{\text{dust}} = T_{\text{exc}, [\text{C}_1]}$ and, moreover, the derivation of the latter requires several assumptions (notably that $[\text{C}_1]$ is in LTE, which are not a given).

⁴ The dust optical depth $\tau = \Sigma_d \kappa_d$, where Σ_d is the dust mass surface density and κ_d the dust opacity, and the wavelength where the dust becomes optically thick is thus $\lambda(\tau = 1) = (\Sigma_d \kappa_{d,0})^{1/\beta} \lambda_0$.

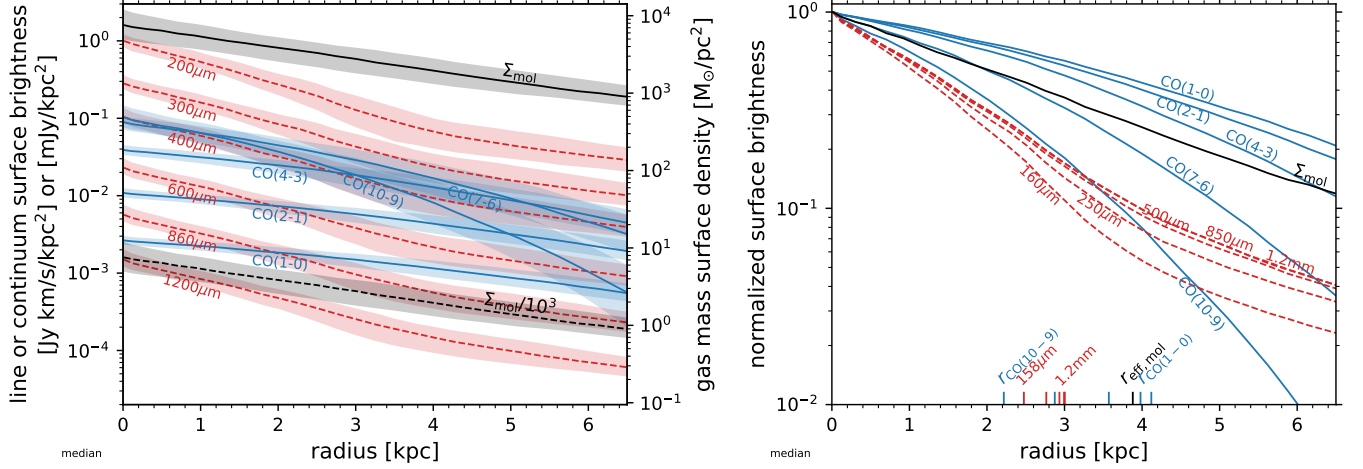


Figure 8. **Left:** Median CO (blue) and dust (red) continuum surface brightness profiles from best-fit model together with the underlying gas mass surface density (black). **Right:** Same figure as on the left but now normalized to the values in the center. The measured effective (half-light) radii are indicated on the x-axis (with the lowest and highest-frequency line and transition labeled).

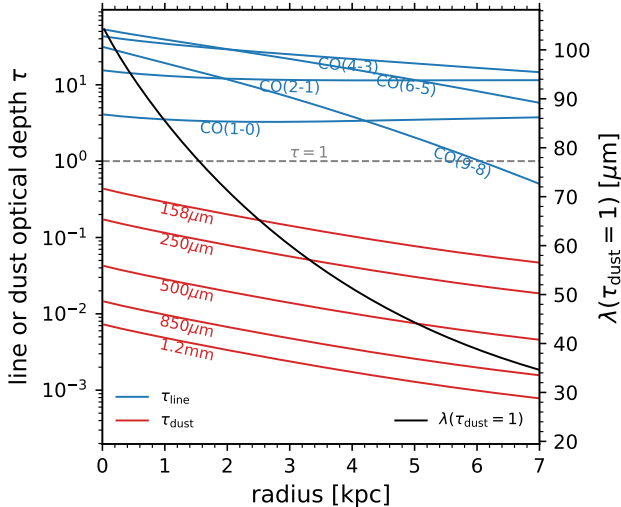


Figure 9. The radial line and continuum optical depths (blue and red lines, left axis) and rest-frame wavelengths where the optical depth reaches unity from the TED model (black line, right axis). The low- J CO lines are optically thick throughout. The dust is mostly optically thin at rest-frame wavelengths longer than 100 μm, but becomes optically thick at those wavelengths in the center.

We stress that the exact profiles and opacities that result from the model are sensitive to the model assumptions as well as systematics in the datasets and should not be overinterpreted. However, the qualitative results explaining the observed radial profiles and the lower dust optical depth stand. A simple test distributing the total dust mass derived from the models over the NOEMA 1.1 mm map (that is, assuming this is a dust-mass map, which is an upper limit on the actual central opacity in the case of dust temperature gradients) shows $\lambda(\tau = 1) \approx 140 \mu\text{m}$ in the central pixel, confirming that it is hard to conceive that global average optical depth is that high.

The picture that emerges is as follows: while GN20 indeed has a very large dust mass, it also hosts a substantial disk, and the dust mass distribution in GN20 is quite extended. As a result, while global dust columns are large, they are also not exceptionally large, as seen, for example, on small scales in the nuclei of some galaxies (e.g., Arp 220; Scoville et al. 2017). The dust column densities and H₂-column densities predicted by the model are still substantial, of order $N_{\text{H}_2} \approx 10^{23} \text{ cm}^{-2}$. These imply an extinction of $A_V \approx 23$ magnitudes (Bohlin & Drake 1978; Güver & Özel 2009), consistent with values derived from Paα (Bik et al. 2024), and ample to completely obscure GN20 in the rest-frame optical.

6. CONCLUSIONS

We present sensitive and high resolution NOEMA imaging at 0.9–1.6 kpc resolution (0''.13–0''.23) of the extended dust continuum emission at 1.1 mm (rest-frame 220 μm) in the $z = 4.055$ dusty star-forming galaxy GN20. Together with JWST/MIRI and NIRCam imaging, that now resolves the (previously-obscured) morphology in the rest-frame optical, near- and mid-infrared, we study the distribution of gas, dust and stars in this prototypical dusty starburst galaxy.

The main conclusions of this paper are as follows:

- The 1.1 mm dust emission is extended and now detected over the full stellar and molecular gas disk of GN20, sharing a common center. The dust emission stretches ≈14 kpc in diameter on its longest axis and is centrally asymmetric and clumpy, with $r_e \approx 2.5 \text{ kpc}$ and $b/a = 0.5$, being brightest in the strongly obscured part of the galaxy. Only 60% of the total dust emission arises from the central $3.5 \times 1.5 \text{ kpc}$ (0''.5–0''.2) and one-third from the nucleus and the prominent clump to the south, implying the starburst is very extended.

- NIRCam and MIRI imaging in the rest-frame optical and near-infrared reveal a clear arm or tidal tail feature in the disk of GN20, the outskirts of the latter coincide with the least-obscured western part of the galaxy detected in the UV/optical. The dust emission in the center is asymmetric and bar-shaped, with a bright dust clump at the tip. There is a prominent gap in the stellar emission between the arm and the nucleus, that is likely a real depression and not due to extinction, supported by the lack of elevated dust emission. Together with the offset nucleus, the presence of nearby companions and the location in a protocluster, this strongly supports GN20 having experienced a recent interaction or merger, which has likely invigorated the starburst.
 - We perform self-consistent radiative transfer modeling of the CO and dust-continuum emission using the Turbulent Non-Equilibrium Radiative Transfer (TUNER) model to derive the molecular gas and dust masses of the system. Interestingly, under the assumed [Draine et al. \(2014\)](#) dust opacity, we find a low (super-solar) gas-to-dust ratio of $\delta_{\text{GDR}} \approx 50$ (and a correspondingly high dust mass $\approx 5.8 \times 10^9 M_\odot$) with an approximately solar CO abundance ($[\text{CO}/\text{H}_2] \approx 10^{-4}$). This may indicate significantly different dust properties in the dust-rich starburst.
 - The radial surface brightness profiles of the CO and near-IR stellar emission are similar ($r_e \approx 4 \text{ kpc}$), suggesting a roughly constant gas fraction across the GN20 disk. In contrast, the dust emission appears significantly more concentrated ($r_e \approx 2.5 \text{ kpc}$). By coupling the TUNER model to a Sérsic column density distribution with radially decreasing linear temperature gradient, we show that this does not mean that the dust is intrinsically more compact. Instead, the profiles can be naturally explained by differences in the radiative transfer between the (mostly) optically thin dust and optically thick CO. The observations are consistent with the gas and dust mass being similarly distributed throughout the starburst.
 - From the combined modeling of the unresolved CO and dust SED together with the resolved radial profiles, we derive a total molecular gas mass in GN20 of $M_{\text{mol}} \approx 2.9^{+0.4}_{-0.3} \times 10^{11} M_\odot$ with an $\alpha_{\text{CO}} = 2.8^{+0.5}_{-0.3}$. Given the dynamical mass of $\approx 5 \times 10^{11} M_\odot$, this implies GN20 is predominately molecular gas rich.
 - We find the dust emission is globally optically thick at wavelengths $\leq 100 \mu\text{m}$, lower than previously reported by [Cortzen et al. \(2020\)](#), but consistent with the extended dust distribution and sufficiently high dust column densities to completely obscure GN20 in the rest-frame optical.
- This study demonstrates the incredible combined power of JWST and (sub)mm interferometers like NOEMA and ALMA to resolve the stellar, gas and dust structure of dusty star-forming galaxies in the early universe. However, our work shows that it remains imperative to carefully consider radiative transfer effects when comparing molecular gas and dust distributions from different tracers. Future studies leveraging deep and high-resolution (sub)mm observations, such as the ALMA Large Programs CONDOR (2024.1.00100.L) and HIDING in the HUDF (2025.1.01377.L), will be able to resolve the gas, dust and stars in more typical early galaxies.
- 1 We thank the referee for a constructive report that
2 helped improve the paper. We are grateful to Luca
3 Costantin for providing the NIRCam imaging. We are
4 also grateful to Hannah Übler for providing the H α
5 map. L.A.B. acknowledges support from the Dutch
6 Research Council (NWO) under grant VI.Veni.242.055
7 (<https://doi.org/10.61686/LAJVP77714>). L.A.B. and J.H.
8 acknowledge support from the ERC Consolidator grant
9 101088676 ("VOYAJ"). L.C. acknowledges support by
10 grant PIB2021-127718NB-100 from the Spanish Min-
11 istry of Science and Innovation/State Agency of Research
12 MCIN/AEI/10.13039/501100011033 and by "ERDF A way
13 of making Europe. A.C.G. acknowledges support by JWST
14 contract B0215/JWST-GO-02926. A.B. and G.O. acknowl-
15 edges support from the Swedish National Space Administra-
16 tion (SNSA). This work is based on observations carried out
17 under project number W22DU with the IRAM NOEMA Inter-
18 ferometer. IRAM is supported by INSU/CNRS (France),
19 MPG (Germany) and IGN (Spain). Some of the data pre-
20 sented in this article were obtained from the Mikulski Archive
21 for Space Telescopes (MAST) at the Space Telescope Science
22 Institute. The specific observations analyzed can be accessed
23 via doi:[10.17909/mrb8-x762](https://doi.org/10.17909/mrb8-x762).

Facilities: NOEMA (IRAM)

Software: TOPCAT ([Taylor 2005](#)), GNUASTRO ([Akhlaghi & Ichikawa 2015](#)), IPYTHON ([Perez & Granger 2007](#)), NUMPY ([Harris et al. 2020](#)), SCIPY ([Virtanen et al. 2020](#)), MATPLOTLIB ([Hunter 2007](#)), ASTROPY ([The Astropy Collaboration et al. 2022](#)), PHOTUTILS ([Bradley et al. 2022](#)), SPECTRALCUBE ([Ginsburg et al. 2019](#)), INTERFEROPY ([Boogaard et al. 2021](#)).

REFERENCES

- Akhlaghi, M., & Ichikawa, T. 2015, ApJS, 220, 1, doi: [10.1088/0067-0049/220/1/1](https://doi.org/10.1088/0067-0049/220/1/1)
- Álvarez-Márquez, J., Crespo Gómez, A., Colina, L., et al. 2023, A&A, 671, doi: [10.1051/0004-6361/202245400](https://doi.org/10.1051/0004-6361/202245400)
- Asplund, M., Grevesse, N., Sauval, A. J., & Scott, P. 2009, ARA&A, 47, 481, doi: [10.1146/annurev.astro.46.060407.145222](https://doi.org/10.1146/annurev.astro.46.060407.145222)
- Bagley, M. B., Finkelstein, S. L., Koekemoer, A. M., et al. 2023, ApJL, 946, L12, doi: [10.3847/2041-8213/acbb08](https://doi.org/10.3847/2041-8213/acbb08)
- Bik, A., Alvarez-Marquez, J., Colina, L., et al. 2024, A&A, 686, 1, doi: [10.1051/0004-6361/202348845](https://doi.org/10.1051/0004-6361/202348845)
- Bohlin, S., & Drake. 1978, ApJ, 132
- Boogaard, L., Meyer, R. A., & Novak, M. 2021, Interferopy: analysing datacubes from radio-to-submm observations, doi: [10.5281/ZENODO.5775603](https://doi.org/10.5281/ZENODO.5775603)
- Boogaard, L. A., Gillman, S., Melinder, J., et al. 2024, ApJ, 969, 27, doi: [10.3847/1538-4357/ad43e5](https://doi.org/10.3847/1538-4357/ad43e5)
- Bradley, L., Sipőcz, B., Robitaille, T., et al. 2022, astropy/photutils: 1.6.0, Zenodo, doi: [10.5281/zenodo.7419741](https://doi.org/10.5281/zenodo.7419741)
- Calistro Rivera, G., Hodge, J. A., Smail, I., et al. 2018, ApJ, 863, 56, doi: [10.3847/1538-4357/aacffa](https://doi.org/10.3847/1538-4357/aacffa)
- Carilli, C. L., Hodge, J., Walter, F., et al. 2011, ApJ, 739, L33, doi: [10.1088/2041-8205/739/1/L33](https://doi.org/10.1088/2041-8205/739/1/L33)
- Carilli, C. L., Daddi, E., Riechers, D., et al. 2010, ApJ, 714, 1407, doi: [10.1088/0004-637X/714/2/1407](https://doi.org/10.1088/0004-637X/714/2/1407)
- Casasola, V., Cassarà, L. P., Bianchi, S., et al. 2017, A&A, 605, doi: [10.1051/0004-6361/201731020](https://doi.org/10.1051/0004-6361/201731020)
- Casey, C. M., Narayanan, D., & Cooray, A. 2014, Phys. Rep., 541, 45, doi: [10.1016/j.physrep.2014.02.009](https://doi.org/10.1016/j.physrep.2014.02.009)
- Casey, C. M., Chapman, S. C., Daddi, E., et al. 2009, MNRAS, 400, 670, doi: [10.1111/j.1365-2966.2009.15517.x](https://doi.org/10.1111/j.1365-2966.2009.15517.x)
- Chen, C.-C., Hodge, J. A., Smail, I., et al. 2017, ApJ, 846, 108, doi: [10.3847/1538-4357/aa863a](https://doi.org/10.3847/1538-4357/aa863a)
- Cheng, C., Yan, H., Huang, J.-S., et al. 2022, ApJL, 936, L19, doi: [10.3847/2041-8213/ac8d08](https://doi.org/10.3847/2041-8213/ac8d08)
- Cochrane, R. K., Hayward, C. C., Anglés-Alcázar, D., et al. 2019, MNRAS, 488, 1779, doi: [10.1093/mnras/stz1736](https://doi.org/10.1093/mnras/stz1736)
- Colina, L., Crespo Gómez, A., Álvarez-Márquez, J., et al. 2023, A&A, 673, 1, doi: [10.1051/0004-6361/202346535](https://doi.org/10.1051/0004-6361/202346535)
- Cortzen, I., Magdis, G. E., Valentino, F., et al. 2020, A&A, 634, 1, doi: [10.1051/0004-6361/201937217](https://doi.org/10.1051/0004-6361/201937217)
- Crespo Gómez, A., Colina, L., Álvarez-Márquez, J., et al. 2024, 1, <https://arxiv.org/abs/2402.18672>
- Da Cunha, E., Walter, F., Smail, I. R., et al. 2015, ApJ, 806, 110, doi: [10.1088/0004-637X/806/1/110](https://doi.org/10.1088/0004-637X/806/1/110)
- Daddi, E., Dannerbauer, H., Stern, D., et al. 2009, ApJ, 694, 1517, doi: [10.1088/0004-637X/694/2/1517](https://doi.org/10.1088/0004-637X/694/2/1517)
- Daddi, E., Dannerbauer, H., Liu, D., et al. 2015, A&A, 577, A46, doi: [10.1051/0004-6361/201425043](https://doi.org/10.1051/0004-6361/201425043)
- Draine, B. T., Aniano, G., Krause, O., et al. 2014, ApJ, 780, 172, doi: [10.1088/0004-637X/780/2/172](https://doi.org/10.1088/0004-637X/780/2/172)
- Dunne, L., Eales, S., Edmunds, M., et al. 2000, MNRAS, 315, 115, doi: [10.1046/j.1365-8711.2000.03386.x](https://doi.org/10.1046/j.1365-8711.2000.03386.x)
- Foreman-Mackey, D. 2016, J. Open Source Softw., 1, 1, doi: [10.21105/joss.00024](https://doi.org/10.21105/joss.00024)
- Foreman-Mackey, D., Hogg, D. W., Lang, D., & Goodman, J. 2013, PASP, 125, 306, doi: [10.1086/670067](https://doi.org/10.1086/670067)
- Frerking, M. A., Langer, W. D., & Wilson, R. W. 1982, ApJ, 262, 590, doi: [10.1086/160451](https://doi.org/10.1086/160451)
- Galametz, M., Kennicutt, R. C., Albrecht, M., et al. 2012, MNRAS, 425, 763, doi: [10.1111/j.1365-2966.2012.21667.x](https://doi.org/10.1111/j.1365-2966.2012.21667.x)
- Gillman, S., Gullberg, B., Brammer, G., et al. 2023, A&A, 676, A26, doi: [10.1051/0004-6361/202346531](https://doi.org/10.1051/0004-6361/202346531)
- Gillman, S., Smail, I., Gullberg, B., et al. 2024, A&A, 691, 1, doi: [10.1051/0004-6361/202451006](https://doi.org/10.1051/0004-6361/202451006)
- Ginsburg, A., Koch, E., Robitaille, T., et al. 2019, radio-astro-tools/spectral-cube: Release v0.4.5, Zenodo, doi: [10.5281/zenodo.3558614](https://doi.org/10.5281/zenodo.3558614)
- Girard, M., Fisher, D. B., Bolatto, A. D., et al. 2021, ApJ, 909, 12, doi: [10.3847/1538-4357/abd5b9](https://doi.org/10.3847/1538-4357/abd5b9)
- Goldsmith, P. F. 2001, ApJ, 557, 736, doi: [10.1086/322255](https://doi.org/10.1086/322255)
- Goodman, J., & Weare, J. 2010, Commun. Appl. Math. Comput. Sci., 5, 65, doi: [10.2140/camcos.2010.5.65](https://doi.org/10.2140/camcos.2010.5.65)
- Greve, T. R., Papadopoulos, P. P., Gao, Y., & Radford, S. J. 2009, ApJ, 692, 1432, doi: [10.1088/0004-637X/692/2/1432](https://doi.org/10.1088/0004-637X/692/2/1432)
- Gullberg, B., Smail, I., Swinbank, A. M., et al. 2019, MNRAS, 490, 4956, doi: [10.1093/mnras/stz2835](https://doi.org/10.1093/mnras/stz2835)
- Güver, T., & Özel, F. 2009, MNRAS, 400, 2050, doi: [10.1111/j.1365-2966.2009.15598.x](https://doi.org/10.1111/j.1365-2966.2009.15598.x)
- Harrington, K. C., Weiss, A., Yun, M. S., et al. 2021, ApJ, 908, 95, doi: [10.3847/1538-4357/abcc01](https://doi.org/10.3847/1538-4357/abcc01)
- Harris, C. R., Millman, K. J., van der Walt, S. J., et al. 2020, Nature, 585, 357, doi: [10.1038/s41586-020-2649-2](https://doi.org/10.1038/s41586-020-2649-2)
- Hodge, J. A., Carilli, C. L., Walter, F., et al. 2012, ApJ, 760, 11, doi: [10.1088/0004-637X/760/1/11](https://doi.org/10.1088/0004-637X/760/1/11)
- Hodge, J. A., & da Cunha, E. 2020, R. Soc. Open Sci., 7, 200556, doi: [10.1098/rsos.200556](https://doi.org/10.1098/rsos.200556)
- Hodge, J. A., Riechers, D., Decarli, R., et al. 2015, ApJ, 798, L18, doi: [10.1088/2041-8205/798/1/L18](https://doi.org/10.1088/2041-8205/798/1/L18)
- Hodge, J. A., Swinbank, A. M., Simpson, J. M., et al. 2016, ApJ, 833, 103, doi: [10.3847/1538-4357/833/1/103](https://doi.org/10.3847/1538-4357/833/1/103)
- Hodge, J. A., da Cunha, E., Kendrew, S., et al. 2025, ApJ, 978, 165, doi: [10.3847/1538-4357/ad9a52](https://doi.org/10.3847/1538-4357/ad9a52)
- Huang, J. S., Li, Z.-J., Cheng, C., et al. 2023, <https://arxiv.org/abs/2304.01378>
- Hunter, J. D. 2007, Comput. Sci. Eng., 9, 90, doi: [10.1109/MCSE.2007.55](https://doi.org/10.1109/MCSE.2007.55)

- Ikeda, R., Tadaki, K.-i., Iono, D., et al. 2022, ApJ, 933, 11, doi: [10.3847/1538-4357/ac6cdc](https://doi.org/10.3847/1538-4357/ac6cdc)
- Kolupuri, S., Decarli, R., Neri, R., et al. 2025, A&A, 695, A201, doi: [10.1051/0004-6361/202452374](https://doi.org/10.1051/0004-6361/202452374)
- Krumholz, M. R., & McKee, C. F. 2005, ApJ, 630, 250, doi: [10.1086/431734](https://doi.org/10.1086/431734)
- Lacy, J. H., Sneden, C., Kim, H., & Jaffe, D. T. 2017, ApJ, 838, 66, doi: [10.3847/1538-4357/aa6247](https://doi.org/10.3847/1538-4357/aa6247)
- Leroy, A. K., Usero, A., Schruba, A., et al. 2017, ApJ, 835, 217, doi: [10.3847/1538-4357/835/2/217](https://doi.org/10.3847/1538-4357/835/2/217)
- Li, A., & Draine, B. T. 2001, ApJ, 554, 778, doi: [10.1086/323147](https://doi.org/10.1086/323147)
- Magdis, G. E., Daddi, E., Elbaz, D., et al. 2011, ApJ, 740, L15, doi: [10.1088/2041-8205/740/1/L15](https://doi.org/10.1088/2041-8205/740/1/L15)
- Maseda, M. V., de Graaff, A., Franx, M., et al. 2024, A&A, 689, A73, doi: [10.1051/0004-6361/202449914](https://doi.org/10.1051/0004-6361/202449914)
- Padoan, P., & Nordlund, A. 2002, ApJ, 576, 870, doi: [10.1086/341790](https://doi.org/10.1086/341790)
- Patra, S., Evans, N. J., Kim, K.-T., et al. 2025, ApJ, 983, 133, doi: [10.3847/1538-4357/adbf8d](https://doi.org/10.3847/1538-4357/adbf8d)
- Peng, C. Y., Ho, L. C., Impey, C. D., & Rix, H.-W. 2002, AJ, 124, 266, doi: [10.1086/340952](https://doi.org/10.1086/340952)
- Perera, T. A., Chapin, E. L., Austermann, J. E., et al. 2008, MNRAS, 391, 1227, doi: [10.1111/j.1365-2966.2008.13902.x](https://doi.org/10.1111/j.1365-2966.2008.13902.x)
- Perez, F., & Granger, B. E. 2007, Comput. Sci. Eng., 9, 21, doi: [10.1109/MCSE.2007.53](https://doi.org/10.1109/MCSE.2007.53)
- Pérez-González, P. G., Costantin, L., Langeroodi, D., et al. 2023, ApJL, 951, L1, doi: [10.3847/2041-8213/acd9d0](https://doi.org/10.3847/2041-8213/acd9d0)
- Planck Collaboration, Aghanim, N., Akrami, Y., et al. 2020, A&A, 641, A6, doi: [10.1051/0004-6361/201833910](https://doi.org/10.1051/0004-6361/201833910)
- Pope, A., Borys, C., Scott, D., et al. 2005, MNRAS, 358, 149, doi: [10.1111/j.1365-2966.2005.08759.x](https://doi.org/10.1111/j.1365-2966.2005.08759.x)
- Pope, A., Scott, D., Dickinson, M., et al. 2006, MNRAS, 370, 1185, doi: [10.1111/j.1365-2966.2006.10575.x](https://doi.org/10.1111/j.1365-2966.2006.10575.x)
- Popping, G., Pillepich, A., Calistro Rivera, G., et al. 2022, MNRAS, 510, 3321, doi: [10.1093/mnras/stab3312](https://doi.org/10.1093/mnras/stab3312)
- Rémy-Ruyer, A., Madden, S. C., Galliano, F., et al. 2014, A&A, 563, A31, doi: [10.1051/0004-6361/201322803](https://doi.org/10.1051/0004-6361/201322803)
- Riechers, D. A., Pope, A., Daddi, E., et al. 2014, ApJ, 786, doi: [10.1088/0004-637X/786/1/31](https://doi.org/10.1088/0004-637X/786/1/31)
- Rizzo, F., Bacchini, C., Kohandel, M., et al. 2024, A&A, 689, A273, doi: [10.1051/0004-6361/202450455](https://doi.org/10.1051/0004-6361/202450455)
- Sandstrom, K. M., Leroy, A. K., Walter, F., et al. 2013, ApJ, 777, 5, doi: [10.1088/0004-637X/777/1/5](https://doi.org/10.1088/0004-637X/777/1/5)
- Scoville, N., Lee, N., Bout, P. V., et al. 2017, ApJ, 837, 150, doi: [10.3847/1538-4357/aa61a0](https://doi.org/10.3847/1538-4357/aa61a0)
- Sérsic, J. 1963, Bol. la Asoc. Argentina Astron. La Plata Argentina, 6, 41
- Sérsic, J. L. 1968, Atlas de Galaxias Australes
- Simpson, J. M., Smail, I., Swinbank, A. M., et al. 2015, ApJ, 799, doi: [10.1088/0004-637X/799/1/81](https://doi.org/10.1088/0004-637X/799/1/81)
- Sofia, U. J., Lauroesch, J. T., Meyer, D. M., & Cartledge, S. I. B. 2004, ApJ, 605, 272, doi: [10.1086/382592](https://doi.org/10.1086/382592)
- Sokal, A. D. 1996, <https://api.semanticscholar.org/CorpusID:14817657>
- Tadaki, K.-i., Kodama, T., Koyama, Y., et al. 2023, ApJL, 957, L15, doi: [10.3847/2041-8213/ad03f2](https://doi.org/10.3847/2041-8213/ad03f2)
- Tadaki, K.-i., Belli, S., Burkert, A., et al. 2020, ApJ, 901, 74, doi: [10.3847/1538-4357/abaf4a](https://doi.org/10.3847/1538-4357/abaf4a)
- Tan, Q., Daddi, E., Magdis, G., et al. 2014, A&A, 569, A98, doi: [10.1051/0004-6361/201423905](https://doi.org/10.1051/0004-6361/201423905)
- Taylor, M. B. 2005, Astron. Data Anal. Softw. Syst. XIV, 347, 29, <https://ui.adsabs.harvard.edu/abs/2005ASPC..347..29T>
- The Astropy Collaboration, Price-Whelan, A. M., Lim, P. L., et al. 2022, ApJ, 935, 167, doi: [10.3847/1538-4357/ac7c74](https://doi.org/10.3847/1538-4357/ac7c74)
- Übler, H., D'Eugenio, F., Perna, M., et al. 2024, MNRAS, 533, 4287, doi: [10.1093/mnras/stae1993](https://doi.org/10.1093/mnras/stae1993)
- van der Tak, F. F. S., Black, J. H., Schöier, F. L., Jansen, D. J., & van Dishoeck, E. F. 2007, A&A, 468, 627, doi: [10.1051/0004-6361:20066820](https://doi.org/10.1051/0004-6361:20066820)
- van der Wel, A., Bell, E. F., Häussler, B., et al. 2012, ApJS, 203, 24, doi: [10.1088/0067-0049/203/2/24](https://doi.org/10.1088/0067-0049/203/2/24)
- Virtanen, P., Gommers, R., Oliphant, T. E., et al. 2020, Nat. Methods, 17, 261, doi: [10.1038/s41592-019-0686-2](https://doi.org/10.1038/s41592-019-0686-2)
- Weiß, A., Downes, D., Neri, R., et al. 2007, Astronomy, 969, 955, doi: [10.1051/0004-6361](https://doi.org/10.1051/0004-6361)

APPENDIX

A. TURBULENT NON-EQUILIBRIUM RADIATIVE TRANSFER (TUNER) MODEL

We perform self-consistent radiative transfer modeling of the CO and dust emission using the Turbulent Non-Equilibrium Radiative Transfer (TUNER) model. The innovation of the TUNER model is that it uses a physically motivated (lognormal) gas density distribution to describe a realistic density distribution with only two parameters, in contrast to two-, or multi-component models that quickly require many more free parameters. An earlier version of the model is described [Harrington et al. \(2021\)](#) and builds directly on the single-component models from [Weiβ et al. \(2007\)](#). The TUNER implementation features a few key differences compared to the earlier works, notably in the implementation of the density distribution, as well as a new Bayesian framework to constrain the posteriors on the parameters.

In brief, we describe the *volume* distribution of H₂ gas (dV) with a lognormal probability distribution (dp ; [Padoan & Nordlund 2002](#); [Krumholz & McKee 2005](#)), such that $dV(n_{\text{H}_2}) = dp(n', \Delta v_{\text{turb}})$, where $n' = n_{\text{H}_2}/\bar{n}_{\text{H}_2}$ is the mean density and Δv_{turb} the turbulent velocity width that defines the width of the distribution via the Mach number ($\mathcal{M} = \Delta v_{\text{turb}}/\sqrt{8 \ln 2/c_s}$, with c_s the sound speed). The density distribution is by default sampled by 50 components on a grid between 10^0 – 10^{10} cm⁻³. The volume of each component i is equal to its equivalent path length under the LVG assumption ($\ell_{\text{equiv}} = \Delta v_{\text{turb}}/(dv/dr)$, where dv/dr [km s⁻¹] = $3.1 \kappa_{\text{vir}} \sqrt{n_{\text{H}_2}}$ [cm⁻³]/ 10^4 , with virial parameter κ_{vir} ; [Goldsmith 2001](#); [Greve et al. 2009](#)) times the fractional source solid angle, $V_i = \Omega_i \ell_{\text{equiv},i}$, such that the full distribution provides the total flux over the full source solid angle (parameterized by radius r via $\Omega_s = \pi(r/D_A(z))^2$, with $D_A(z)$ the angular diameter distance at redshift z). The CO and dust are coupled to the H₂ distribution via a single [CO/H₂] abundance and gas-to-dust ratio, δ_{GDR} . The gas and dust temperatures are not fixed to be isothermal (e.g. [Leroy et al. 2017](#)) but are allowed to vary as a power law with density, $T(n_{\text{H}_2}) \propto n_{\text{H}_2}^{\gamma_T}$, where typically $\gamma_T \leq 0$, such that denser gas is colder, and zero implying isothermal gas. The T_{kin} and T_{dust} temperatures are normalized such that the volume weighted means correspond to the input temperatures. The observed continuum and line emission (in contrast against the background) can be derived from the equation of radia-

tive transfer:

$$S_{\nu}^{\text{cont,obs}} = \frac{\Omega_s}{(1+z)^3} (B_{\nu}(T_{\text{dust}}) - B_{\nu}(T_{\text{CMB}}(z))) (1 - e^{-\tau_{\nu}}) \quad (\text{A1})$$

$$S_{\nu_L}^{\text{line,obs}} = \frac{\Omega_s}{(1+z)^3} (B_{\nu_L,\text{bg}}(T_{\text{exc}}) - I_{\nu_L,\text{bg}}(z)) (1 - e^{-\tau_{\nu_L}}), \quad (\text{A2})$$

where $B_{\nu}(T)$ is Planck blackbody function at the relevant continuum or line frequency and temperature and τ_{ν} is the corresponding optical depth. The excitation temperatures (T_{exc}), optical depths and line fluxes of each density component are solved using the LVG approximation and a geometrically averaged escape probability $p_{\text{esc}} = (1 - e^{-\tau_{\nu_L}})/\tau_{\nu_L}$ (cf. RADEX; [van der Tak et al. 2007](#)) as described in [Weiβ et al. 2007](#)). The background radiation field ($I_{\nu_L,\text{bg}}(z)$) is equal to half that of the dust (assuming complete mixing) plus the Cosmic Microwave Background (CMB) at the redshift of interest. The model assumes a default temperature floor of 10 K above T_{CMB} , to avoid hiding material that is invisible in contrast to the CMB. The dust opacity is described using the typical power-law assumption $\kappa_{\nu} = \kappa_0(\nu/\nu_0)^{\beta}$. The total mass of the system is equal to the sum of the mass of the individual components, which is derived as described in [Weiβ et al. \(2007\)](#).

We derive the posteriors using emcee ([Foreman-Mackey et al. 2013](#)) that uses the affine invariant sampler from [Goodman & Weare \(2010\)](#). We assess whether the sampling has sufficiently converged, running the chains until the estimates of the integrated autocorrelation time τ ([Sokal 1996](#)) have settled to within 5% and the length of the chains are at least 50τ . For efficiency reasons we only store the posterior during optimization and recompute the full model output for a representative subset of posterior samples which is used for further analysis.

B. TABLES AND CORNER PLOTS

Continuum and line flux measurements for GN20 are reported in [Table 1](#). Corner plots of the posteriors for the models shown in [Fig. 6](#) (§ 4.1) and [Fig. 7](#) (§ 4.2) are shown in [Fig. 10](#) and [Fig. 11](#) respectively. The associated marginalized constraints on the parameters are tabulated in [Table 2](#) and [Table 3](#).

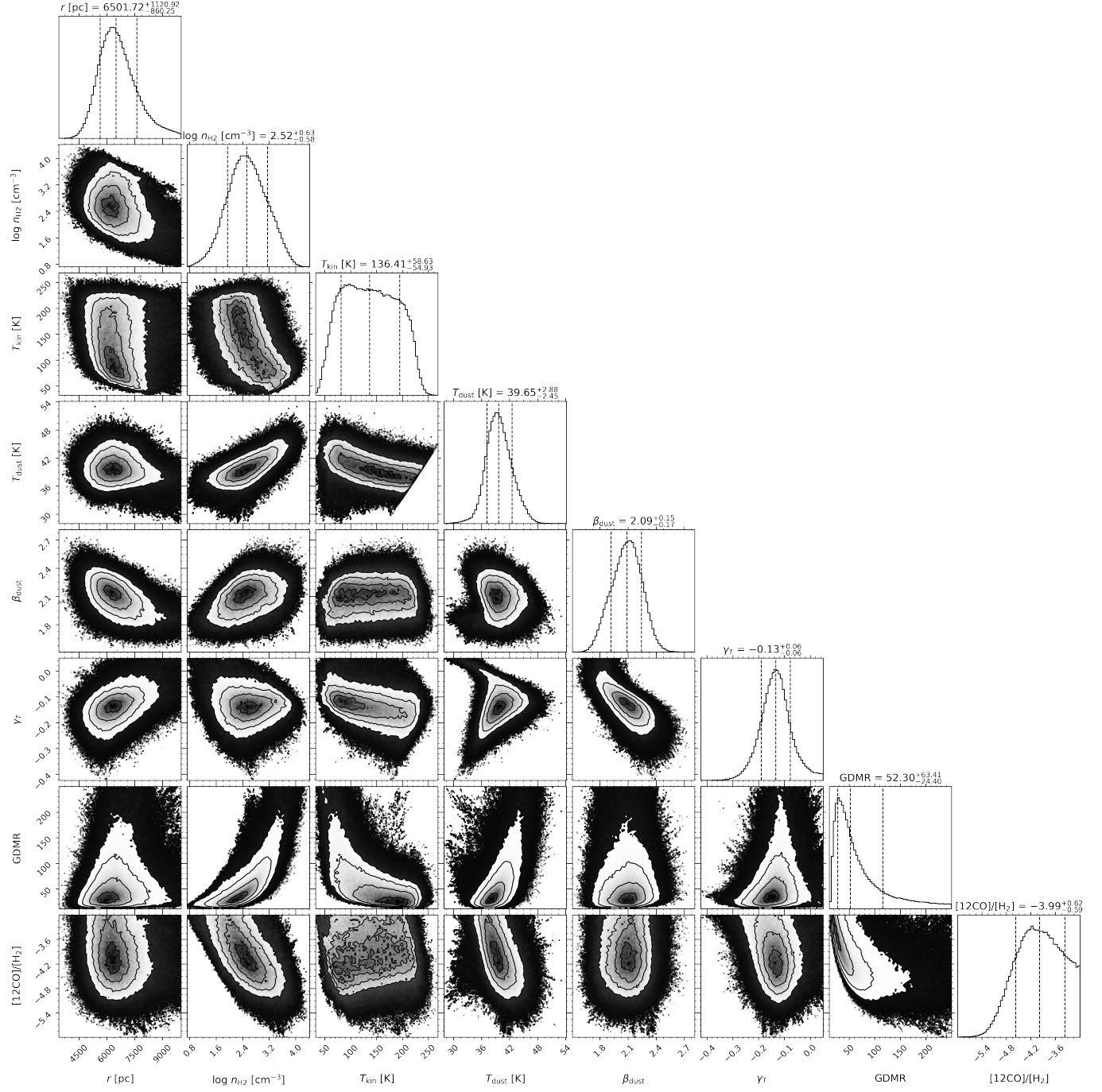


Figure 10. Corner plot (Foreman-Mackey 2016) of the posterior for the TUNER model (§ 4.1, see Fig. 6). The top panels show the 1D marginalized posteriors with the median and 16th- and 84th-percentiles, while the lower panels show the 2D marginalized covariances.

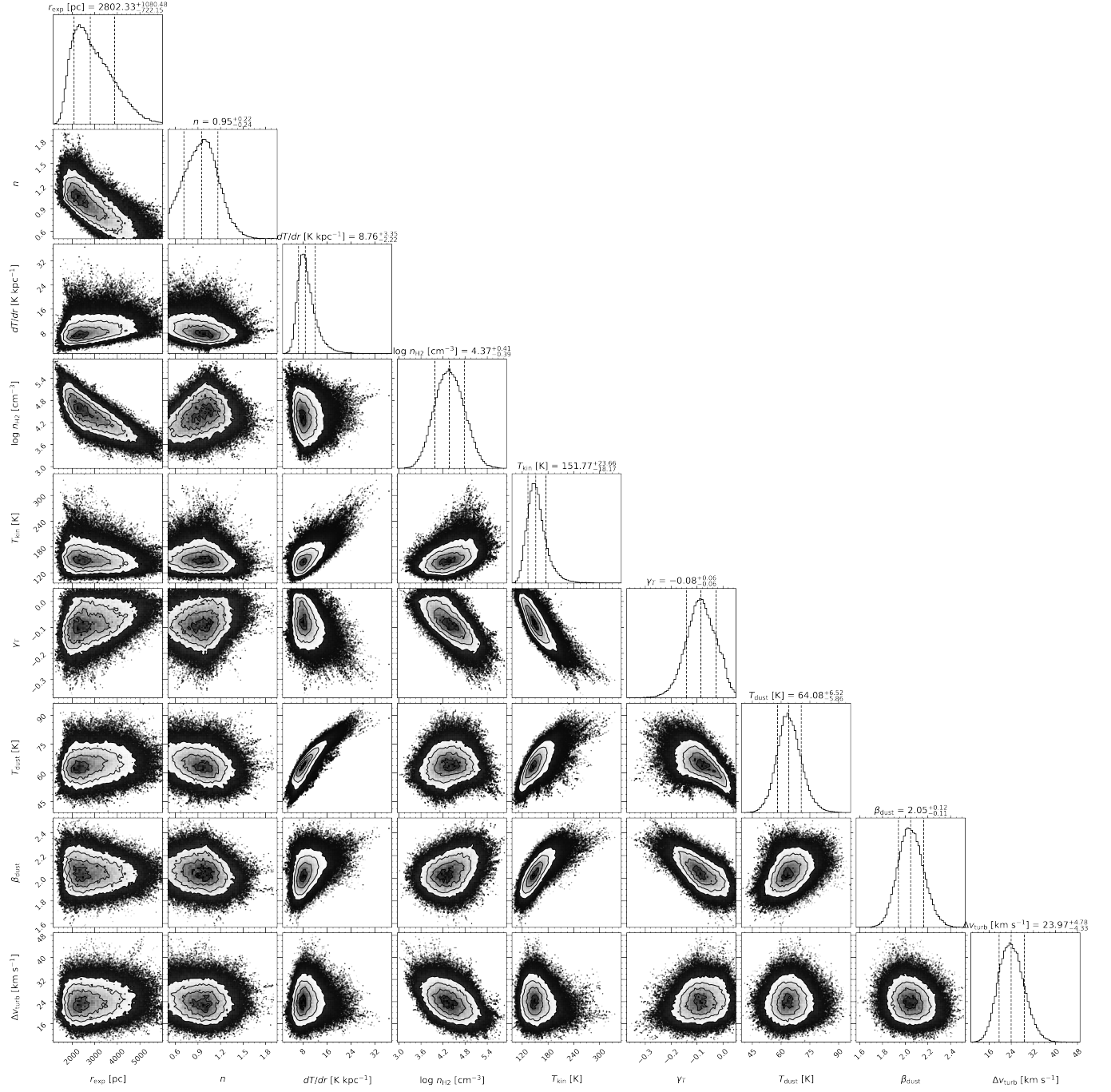


Figure 11. Corner plot (Foreman-Mackey 2016) of the posterior for the TED model (§ 4.2, see Fig. 7). The top panels show the 1D marginalized posteriors with the median and 16th- and 84th percentiles, while the lower panels show the 2D marginalized covariances. Note the scale radius r_{exp} is different from the effective- or half-light radius, which is instead computed a posteriori.

Table 1. GN20 continuum and line measurements.

Parameter	Value	Reference
$S_{3.3\text{ mm}}$	0.23 ± 0.04 mJy	T14
$S_{3.05\text{ mm}}$	0.36 ± 0.04 mJy	C20
$S_{2.2\text{ mm}}$	0.95 ± 0.14 mJy	T14
$S_{1.86\text{ mm}}$	2.8 ± 0.13 mJy	C20
$S_{1.2\text{ mm}}$	8.47 ± 0.79 mJy	T14
$S_{1.1\text{ mm}}$	11.5 ± 0.2 mJy	This work
$S_{1.1\text{ mm}}$	11.5 ± 1.5 mJy	P08
$S_{880\mu\text{m}}$	18.0 ± 1.0 mJy	H15
$S_{850\mu\text{m}}$	20.3 ± 2.0 mJy	P06, M11
$S_{500\mu\text{m}}$	39.7 ± 6.1 mJy	M11
$S_{350\mu\text{m}}$	41.3 ± 5.2 mJy	M11
$S_{250\mu\text{m}}$	18.66 ± 2.70 mJy	M11, T14
$S_{160\mu\text{m}}^{\dagger}$	5.45 ± 1.02 mJy	M11, T14
$S_{100\mu\text{m}}^{\dagger}$	0.70 ± 0.24 mJy	M11, T14
$I_{\text{CO}(1-0)}$	0.21 ± 0.05 Jy km s $^{-1}$	C10
$I_{\text{CO}(2-1)}$	0.64 ± 0.16 Jy km s $^{-1}$	C10
$I_{\text{CO}(2-1)}^{\ddagger}$	0.87 ± 0.09 Jy km s $^{-1}$	C11
$I_{\text{CO}(2-1)}^{\ddagger}$	1.0 ± 0.3 Jy km s $^{-1}$	H12
$I_{\text{CO}(4-3)}$	1.68 ± 0.1 Jy km s $^{-1}$	T14
$I_{\text{CO}(5-4)}$	2.2 ± 0.7 Jy km s $^{-1}$	C10
$I_{\text{CO}(6-5)}$	1.8 ± 0.2 Jy km s $^{-1}$	C10
$I_{\text{CO}(7-6)}$	2.36 ± 0.20 Jy km s $^{-1}$	C20 ^a
$I_{[\text{C I}](1-0)}^{\ddagger}$	0.70 ± 0.11 Jy km s $^{-1}$	C20
$I_{[\text{C I}](2-1)}^{\ddagger}$	1.80 ± 0.21 Jy km s $^{-1}$	C20
$I_{[\text{N II}] 205\mu\text{m}}$	1.80 ± 0.21 Jy km s $^{-1}$	K25

NOTE—[†]Herschel/PACS measurements tracing hot/warm dust are excluded in the modeling. [‡]CO(2–1) measurements based on higher-resolution data and lines other than CO are not used in the modeling, see discussion in § 4. ^aG. Magdis, private communication. The CO(7–6) and [C I](2–1) measurements supersede the inconsistent upper limits from (Casey et al. 2009). References: Pope et al. (2006, P06), Perera et al. (2008, P08), Carilli et al. (2010, C10), Carilli et al. (2011, C11), Magdis et al. (2011, M11), Hodge et al. (2012, H12), Tan et al. (2014, T14), Hodge et al. (2015, H15), Cortzen et al. (2020, C20), Kolupuri et al. (2025, K25).

Table 2. GN20 TUNER model posterior parameter percentiles.

Parameter	Value
r [pc]	6511^{+1345}_{-989}
$\log n_{\text{H}_2}$ [cm $^{-3}$]	$2.64^{+0.63}_{-0.59}$
T_{kin} [K]	$125.8^{+56.1}_{-52.8}$
T_{dust} [K]	$40.2^{+2.9}_{-2.8}$
β_{dust}	$2.08^{+0.15}_{-0.18}$
γ_T	$-0.13^{+0.05}_{-0.05}$
δ_{GDR}	57^{+116}_{-28}
[CO/H ₂] × 10 ⁻⁵	$7.07^{+32.63}_{-4.98}$
$\log n_{\text{H}_2}^{\text{out}}$ [cm $^{-3}$]	$2.82^{+0.53}_{-0.43}$
M_{mol} [10^{11} M_\odot]	$3.46^{+5.91}_{-1.81}$
M_{dust} [10^9 M_\odot]	$5.87^{+0.61}_{-0.97}$
$L'_{\text{CO}(1-0)}$ [10 ¹⁰ K km s $^{-1}$ pc 2]	$9.71^{+1.32}_{-1.36}$
$\alpha_{\text{CO}(1-0)}$ [M $_\odot$ (K km s $^{-1}$ pc 2) $^{-1}$]	$3.56^{+7.26}_{-1.90}$
L_{IR} [10 ¹³ L $_\odot$]	$1.56^{+0.12}_{-0.09}$

NOTE—The parameters are described in § 4 and Appendix A. The mean density of the distribution over the modeled density range is $\log n_{\text{H}_2}^{\text{out}}$ (see Appendix A). The infrared luminosity is integrated over 8–1000 μm.

Table 3. GN20 TED model posterior parameter percentiles.

Parameter	Value
r_{exp} [pc]	2914^{+1245}_{-965}
n	$0.98^{+0.18}_{-0.30}$
dT/dr [K kpc $^{-1}$]	$8.42^{+5.11}_{-2.37}$
$\log n_{\text{H}_2}$ [cm $^{-3}$]	$4.31^{+0.43}_{-0.39}$
T_{kin} [K]	$154.6^{+21.8}_{-21.9}$
γ_T	$-0.08^{+0.06}_{-0.04}$
T_{dust} [K]	$62.7^{+9.7}_{-5.6}$
β_{dust}	$2.06^{+0.07}_{-0.12}$
Δv_{turb} [km s $^{-1}$]	$24.9^{+4.3}_{-3.3}$
$\log n_{\text{H}_2}^{\text{out}}$ [cm $^{-3}$]	$3.78^{+0.44}_{-0.35}$
M_{mol} [10^{11} M_\odot]	$2.87^{+0.39}_{-0.30}$
M_{dust} [10^9 M_\odot]	$5.74^{+0.79}_{-0.60}$
$L'_{\text{CO}(1-0)}$ [10 ¹¹ K km s $^{-1}$ pc 2]	$1.03^{+0.10}_{-0.11}$
$\alpha_{\text{CO}(1-0)}$ [M $_\odot$ (K km s $^{-1}$ pc 2) $^{-1}$]	$2.76^{+0.52}_{-0.34}$
L_{IR} [10 ¹³ L $_\odot$]	$1.64^{+0.13}_{-0.14}$

NOTE—Parameter description in Table 2.